

Hyper-Kamiokande Outer Detector Light Injector System Technical Note

Balint Bogdan*, Sam Jenkins, Neil McCauley, Steve Boyd, Keith Jewkes,
Menai Lamers James, Grace Hannaford, Ankush Mitra, Liz Kneale,
Patrick Stowell

October 1, 2025

5 Contents

| | | |
|----|-----------------------------------------------------------|----|
| 6 | 0 Version history | 3 |
| 7 | 1 Introduction | 4 |
| 8 | 2 Light Injection System Overview and Requirements | 4 |
| 9 | 3 OD PMT Saturation Study | 5 |
| 10 | 3.1 Diffuser Simulation | 6 |
| 11 | 3.2 Diffuser and OD Parameters | 7 |
| 12 | 3.3 Saturation Analysis | 8 |
| 13 | 3.4 Results | 9 |
| 14 | 4 OD Collimator Studies | 11 |
| 15 | 4.1 Collimator Simulation | 11 |
| 16 | 4.2 Collimator Sensitivity Analysis | 13 |
| 17 | 4.3 Results | 13 |
| 18 | 5 Diffuser Design | 15 |
| 19 | 5.1 ID Diffuser Hemisphere Design | 15 |
| 20 | 5.1.1 Inner Detector Diffuser Design | 15 |
| 21 | 5.1.2 Diffuser Profile Measurement System | 15 |
| 22 | 5.1.3 Diffuser Power Measurement System | 15 |
| 23 | 5.2 OD Diffuser Design | 18 |
| 24 | 6 OD Diffuser Mounting System and Installation | 19 |
| 25 | 7 Pulser Board | 20 |
| 26 | 7.1 Pulser Board Overview | 20 |
| 27 | 7.2 Physical Dimensions and Construction | 21 |
| 28 | 7.3 LED | 24 |
| 29 | 7.3.1 Overview | 24 |
| 30 | 7.3.2 Switching Circuit | 24 |

*bbogdan@liverpool.ac.uk

| | | |
|----|---------------------------------------------------|-----------|
| 31 | 7.3.3 Switch Selection | 24 |
| 32 | 7.3.4 Testing | 25 |
| 33 | 7.4 LVDS to TTL Converter | 29 |
| 34 | 7.5 Power Supplies | 30 |
| 35 | 7.6 Connector | 33 |
| 36 | 7.7 Fibre Coupler | 33 |
| 37 | 7.8 Photon Yield Tests | 34 |
| 38 | 7.9 Production | 34 |
| 39 | 7.10 Changes Expected from v0.9 to v1.0 | 34 |
| 40 | 7.10.1 LED and Switching Circuit | 34 |
| 41 | 7.10.2 LVDS-to-TTL Converter | 34 |
| 42 | 7.10.3 Power Supplies | 35 |
| 43 | 7.10.4 Connector | 35 |
| 44 | 7.10.5 Fibre Coupler | 35 |
| 45 | 8 Server Rack and Cooling | 35 |
| 46 | 9 LED Monitoring | 36 |
| 47 | 10 Control System for LEDs | 36 |
| 48 | 11 Crate Electronics | 37 |
| 49 | 11.1 Overview | 37 |
| 50 | 11.2 Blade | 38 |
| 51 | 11.3 Backplane | 38 |
| 52 | 11.4 Eurocard | 39 |
| 53 | 12 Conclusions | 40 |

54 **0 Version history**

- 55 ● v0.99 - First release by Balint circulated to Liverpool group for internal review
56 ● v1 - [Sam]: Ported over to github for continued development, as we hit compilation
57 time on overleaf. Initial pass through to fix wording and rewrite some sections. Also
58 integrating Warwick TN on OD diffuser, and Liz's work on the OD saturation studies.
59 Some reordering of structure to make it flow better.

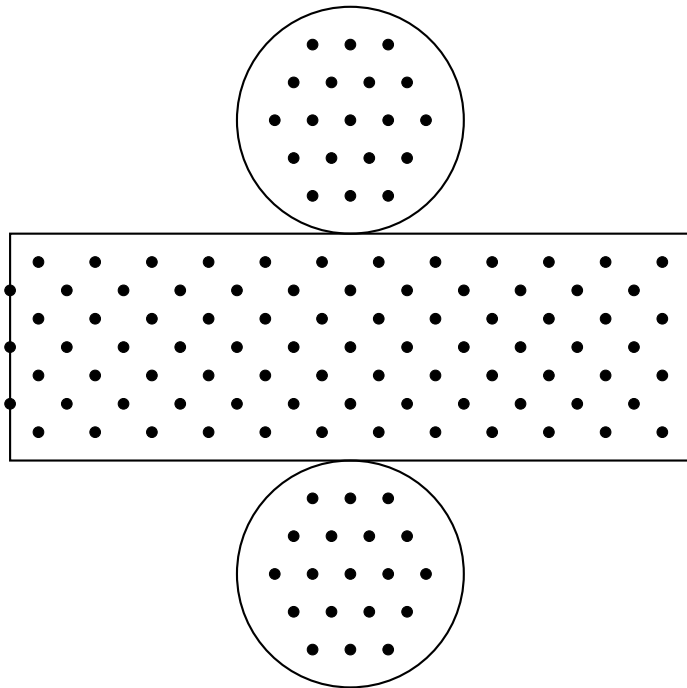
60 **1 Introduction**

61 Hyper-Kamiokande is a large scale water Cherenkov detector with two main sections, an
62 inner detector (ID) and an outer detector (OD). The OD volume of Hyper-K is a one meter
63 wide annular ring on the circumference of the detector. This space is designed to tag charged
64 particles, such as cosmic ray muons or particles from interactions in the surrounding rock,
65 entering the detector. In addition, the OD volume will be used as working space for instal-
66 lation activities. Once complete, it will be optically separated from the ID volume, and will
67 be instrumented with 3,600 outward facing 8 cm photomultipliers tubes (PMTs). These will
68 each surrounded by wavelength shifting (WLS) plates to increase photocoverage.

69 In order to achieve the precision measurements Hyper-K aims to make, precise calibration
70 of the detector is required. For the OD, a light injection (LI) system will be employed,
71 allowing for known quantities of light to be injected into the detector region. This will
72 consist of 122 diffusers and 12 collimators. The diffuser system, which is described in this
73 technical note, will be used to measure gain and timing properties of the OD PMTs, and
74 will be powered by dedicated pulsed LED sources. The 12 OD collimators are identical to
75 those uses in the ID system, and will be integrated into the ID laser system. Full details on
76 that system, along with investigations of the fibre optics that will be employed for the OD
77 system, can be found in [1].

78 **2 Light Injection System Overview and Requirements**

79 The OD diffuser system will be composed of 122 bare diffusers, installed on the outward facing
80 side of the PMT support structure. The proposed layout for this is shown in Figure 1, though
81 in actuality there will be minor differences from this regular arrangement due to restrictions
from other systems. These are arranged such that they illuminate roughly an equal amount



82 Figure 1: Injector location map for OD diffuser positions. Locations are approximate and
83 dependent on PMT/WLS plate locations.

82 of OD PMTs. One of the primary goals of the system is to inject enough light to saturate the
83

84 OD PMTs. This goal drives a large part of the photon output optimisation, and Monte Carlo
85 (MC) studies to evaluate the amount of photons required to do this are shown in Section 3.
86 The diffuser design is discussed in Section 5. These will each be illuminated by individual
87 LED pulser boards with 365 nm LEDs. This will require at least 122 dedicated LED pulsers,
88 and spares should be readily available for hot-swapping should a board encounter issues. Full
89 details of the pulser board design are given in Section 7. The pulser boards will be powered
90 and controlled by commercially-available Field Programmable Grid Array (FPGA) boards.
91 The control system architecture for these consists of three primary components:

- 92 • **Blade:** Interfaces directly with the FPGA, distributing all differential signals into the
93 crate system.
- 94 • **Backplane:** Routes differential signals to the pulser boards and provides the primary
95 power distribution, accepting 12 V and ± 5 V inputs.
- 96 • **Eurocards:** Host the pulser boards, receive power and differential signals from the
97 backplane, and incorporate the necessary circuitry for laser triggering.

98 Further details on the control system and individual electronics crate components are given
99 in Sections 10 and 11 respectively.

100 Light will be transported between the pulsers and diffusers by a series of fibre optic
101 cables; following the investigations in [1] the Thorlabs FP400URT [2] is targeted for this.
102 Due to production limitations, it is not possible to keep all fibre path lengths the same.
103 Instead there will be five different lengths: 50 m, 80 m, 106 m, 124 m and 168 m. The
104 light output after signal attenuation and dispersion in these fibres should be as consistent
105 as possible, which will require fine tuning given the different amounts of attenuation and
106 dispersion which pulses will experience based on fibre length.

107 The initial design requirements for the system are to produce pulse widths out of the
108 diffuser of no more than 10 ns, with a photon yield in the range 1–15 million photons per
109 pulse (ppp). The 10 ns limit is driven by the timing resolution of the WLS plates. The
110 wavelength of light used is also partially dictated by the WLS plates, which will not activate
111 for light above 400 nm. The photon yield target here is more of a goal than a requirement,
112 and saturation studies were performed using numbers motivated by system performance.
113 These are summarised in Section 3.

114 The below paragraph should split up. The first half has been rewritten into the above
115 paragraph, the second should be fleshed out for the photon yield test section. This will be
116 removed once that is done.

117 Pulse width should ideally be between 1-10 ns and the photon count from 1-15 million
118 photons, but higher limits are preferable. The lower limits are not possible to achieve, as the
119 fibre dispersion will create a minimum pulse width, which is 4.5 ns at 180 metres, and if we
120 try to achieve large light output it will compromise our lower light output, so we can only
121 achieve around 100,000 photons per pulse at minimum. While these compromises are not
122 ideal, the fibre selection limits our capabilities on hitting the required theoretical targets.

123 3 OD PMT Saturation Study

124 The light injection system in the OD will use collimated and diffuse light injection to calibrate
125 the PMTs and to measure the optical properties (scattering and absorption) of water, as well
126 as any degradation in Tyvek reflectivity over the course of operation.

127 Diffuse light sources will be used for in-situ calibration of the PMT charge response.
128 Light will be injected at very low levels to measure the single-photoelectron charge response,
129 and the requirement to achieve single-photoelectron coverage across all PMTs was used to

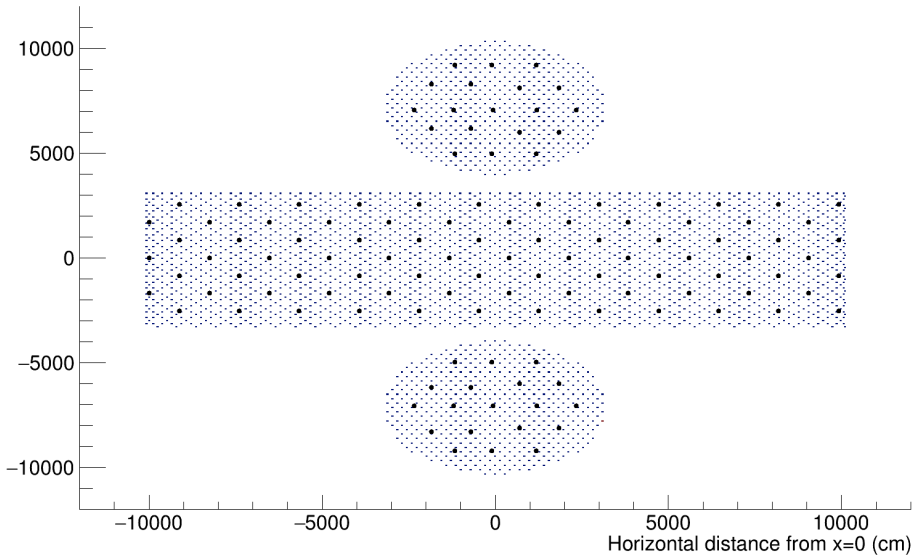


Figure 2: Positions of the OD PMTs and diffuser positions used in the calibration simulations. Note that the positions of PMTs in the top and bottom rows of the barrel have changed in the design, and as such the results presented in this tech note reflect these changes. This differs from the most recent version of WCSim (1.12.26) [4] that has been used as a basis for the simulation, and the changes are reflected in pull request #525.

130 determine the number of light injectors required for the light injection calibration system, as
 131 reported in the Outer Detector Technical Report [3]. In order to calibrate the PMTs across
 132 their entire range, the light injection system must also be capable of illuminating PMTs to
 133 saturation, to understand the change in their response as they approach saturation.

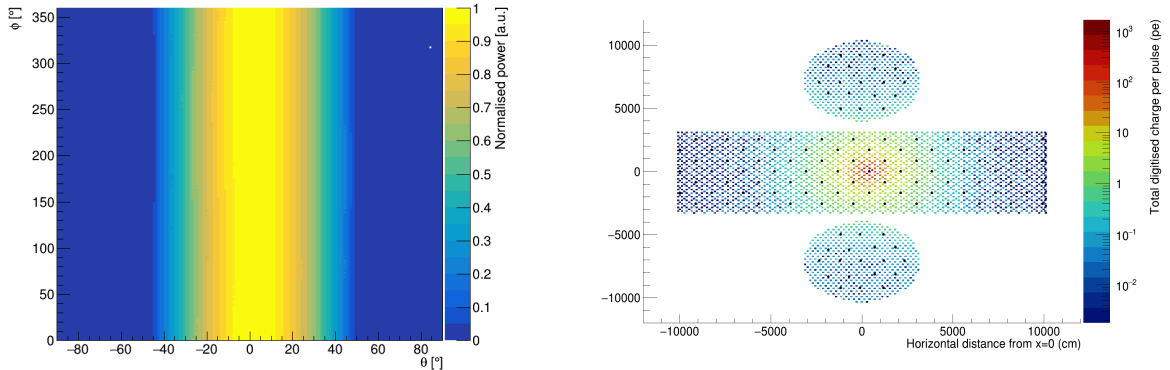
134 This section describes the use of diffuse light injection to evaluate the suitability of light
 135 sources for in-situ measurements of the PMT saturation response. Section 3.1 describes the
 136 diffuser simulation, Section 3.2 gives details of the OD geometry and diffuser parameters
 137 used, and Sections 3.3 and 3.4 describe the scope, analysis and results of the saturation
 138 study.

139 3.1 Diffuser Simulation

140 The planned light injection calibration system will include 122 diffusers, as determined by
 141 maximising the single-photoelectron coverage of all of the OD PMTs [3]. The division of dif-
 142 fusers between the endcaps and barrels, and their positions in terms of the overall geometry,
 143 has been altered since [3], following an update of the design and geometry in the simulation.
 144 Figure 2 shows the updated diffuse light injector (LI) locations with respect to OD PMT
 145 positions. The diffusers have been positioned as close to equidistant as possible from the
 146 surrounding PMTs, next to a strut in an empty cell.

147 A new LI generator has been written within the framework of WCSim [4]. This allows
 148 the user to define the characteristics of the LI within a data file input to the simulation. The
 149 following characteristics can be defined:

- 150 • Global position within the detector geometry,
- 151 • Direction of the LI axis,
- 152 • Wavelength of the optical photons



(a) ID diffuser profile measured in water, used for the diffuser simulations described in this technical report. A measured profile for each diffuser will be stored in the database for OD calibration.

(b) Charge in photoelectrons on each PMT produced when the profile in (a) is used to simulate optical photons from a diffuser pointing outwards in the barrel OD. The size of the PMT + WLS plates has been increased only in the plot for improved visualisation.

Figure 3: Diffuser profile measured in water, and the resulting charge map from this profile.

- 153 • Pulse width
- 154 • Photons per pulse
- 155 • LI profile in the form of arrays of θ , ϕ and measured light intensity, where θ is the
156 angle made with the axis of the LI and ϕ is the rotation around the axis.

The LI profile opening angle and intensity can reflect either a flat angular distribution of photons within the desired angular range of the light injector (-opening angle, +opening angle), or can be drawn from the measured profile for that injector, in which case the LI generator accurately models the variation across the profile, and in particular the drop-off in the frequency of photons towards the edge of the LI profile. For each pulse, the generator samples the specified number of photons per pulse, each with an energy calculated from the wavelength set in a database currently stored within WCSim, and a time sampled from a Gaussian distribution around the mean, with a variance equal to the pulse width specified in the database. Each photon is also assigned a global direction, which is sampled with a distribution corresponding to the LI profile.

The profile of each diffuser will be measured and stored in the database as a function of the diffuser identifier number in the final simulation. For the purposes of the diffuser simulations presented in this tech note, a single profile taken from the measurement of a diffuser profile in water has been used. This diffuser profile corresponds to an opening angle of around 40°. Since the OD diffuser profiles have not yet been measured in water, an ID diffuser profile has been used to approximate a realistic OD diffuser profile. Although the design of the OD diffusers has been modified from the ID diffuser design in order to increase the diffuser efficiency, the design has been shown to maintain the desired profile and as such the ID diffuser profile is expected to be a reasonable approximation. The diffuser profile used, and the resulting charge map from a diffuser in the barrel is shown in Figure 3.

177 3.2 Diffuser and OD Parameters

178 The characteristics of diffusers simulated in the saturation study are summarised in Table I.
179 The number of photons per pulse used in the simulation was based on measurements made

from the LED pulser setup, using a chain of fibre optic cables equating to 181 m in length. The simulations described here use two different values for the number of photons per pulse, corresponding to a maximum photon yield from the fibre optic chain of 11×10^6 photons per pulse and 20×10^6 photons per pulse. This was modified to account for an assumed diffuser efficiency of 50%. As such, the simulated number of photons per pulse simulated is 5.5×10^6 and 10×10^6 respectively.

| Parameter | Assumed value |
|---------------------|----------------------------------|
| Photons per pulse | $11 \times 10^6, 20 \times 10^6$ |
| Wavelength | 365 nm |
| Pulse width | 10 ns |
| Diffuser efficiency | 50% |

Table I: The LI configuration used in the diffuser simulations for the saturation study presented in Section 3.3.

The OD geometry parameters that have been used in the simulations for the saturation study are shown in Table II.

| Parameter | Assumed value |
|------------------------|---------------|
| PMT radius | 8 cm |
| PMT dark rate | 0.4 kHz |
| OD lateral water depth | 1 m |
| OD height water depth | 2 m |
| OD dead space | 60 cm |
| Tyvek sheet thickness | 1 mm |
| WLS plate thickness | 6 mm |
| WLS plate length | 30 cm |

Table II: The OD configuration used for the saturation study presented in Section 3.3 using WCSim version 1.12.26.

3.3 Saturation Analysis

The limit of the PMT range is governed by the electronics response, which is expected to fully saturate at around 100 photoelectrons (pe) in a 16 ns time window. The simulation of the PMT charge response in WCSim does not currently fully handle the saturation, but it is expected that the linearity of the charge response will break down between 80 pe and 100 pe. Saturation measurements aim to measure the PMTs over the full range of this breakdown in linearity. The saturation level for the purposes of this study has been taken to be 100 pe in 16 ns, but the analysis has been designed to take into account the need to measure across the entirety of this range.

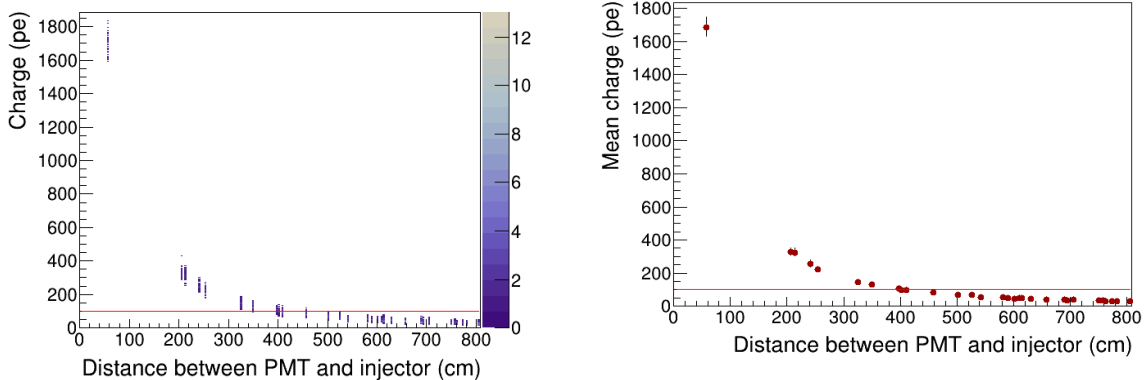
The saturation of OD PMTs has been evaluated in the top endcap, barrel and bottom endcap. The diffuser simulations are intensive, requiring millions of tracked photons to simulate a single flash, and the OD parameters are not yet finalised. As such, only two diffusers in each of the top endcap, barrel and bottom endcap have been simulated for this current study.

Two values have been used as figures of merit to determine the PMT saturation coverage:

- Mean saturation distance - the distance from the nearest diffuser at which the mean charge per PMT is greater than saturation level.

- 205 • Saturation limit - the greatest distance from the nearest diffuser at which the charge
 206 on any PMT reaches the saturation level.

207 For each configuration, the charge per PMT was plotted as a function of the distance
 208 from the nearest diffuser, to give the saturation limit (Figure 4a). The mean saturation
 209 distance was then found by taking the mean of the same plot (Figure 4b). The plot showing
 210 the saturation limit is particularly useful in understanding the range of distances over which
 211 it is possible to see the expected range of breakdown of linearity.



(a) Plot of the charge per PMT as a function of the distance from the nearest diffuser. The saturation limit is the greatest distance at which saturation is achieved i.e. 5.0 m in this case.

(b) Plot of the mean charge per PMT found by taking the mean of the left-hand plot. The mean saturation distance is the greatest distance at which the mean charge per PMT is greater than the saturation level i.e. 4.0 m.

Figure 4: Sample plots showing the mean saturation distance and saturation limit used as figures of merit for the saturation study. The red, horizontal lines mark the assumed saturation level of 100 pe.

212 Since only six diffuser locations have been simulated, the percentage of PMTs within
 213 the mean saturation distance and saturation limit is calculated assuming symmetry both of
 214 the detector and of the diffuser positions with respect to the PMTs. However, for practical
 215 reasons, the diffusers have to be positioned off-centre in the empty cells between PMTs, next
 216 to the struts on the PMT support structure. As such, a full simulation of all diffusers should
 217 be performed in future, once the OD geometry and LI specifications have been finalised, for
 218 an accurate evaluation of the percentage saturation across the whole detector.

219 3.4 Results

220 The mean saturation distance and saturation limit were evaluated for two OD diffuser loca-
 221 tions in each of the top endcap, barrel and bottom endcap. The results for 5.5 M photons per
 222 pulse are shown in Table III, along with the percentage of PMTs within the mean saturation
 223 distance and saturation limit. Table IV shows the mean charge at the calculated saturation
 224 distance and the mean charge at the saturation limit at the six diffuser positions. The results
 225 for 10 M photons per pulse are shown in Table V and Table VI.

226 Figure 5 shows the PMT charge map for the barrel 1 diffuser illuminated by 10 M photons per
 227 pulse, with the saturation distance and saturation limits marked around the barrel PMTs.

228 Due to the differing geometry the mean saturation distance in the barrel (5.4 m for 10 M
 229 photons per pulse) is slightly higher than in the endcaps (4.3-5.5 m), and the percentage
 230 of PMTs within the mean saturation distance in the barrel is higher at 57% than in the
 231 endcaps (37-48%). Similarly, the percentage of PMTs within the saturation limit in the

| OD location | Mean saturation distance | % PMTs within saturation distance | Saturation limit | % PMTs within saturation limit |
|-----------------|--------------------------|-----------------------------------|------------------|--------------------------------|
| Barrel 1 | 4.0 m | 31% | 5.0 m | 50% |
| Barrel 2 | 4.0 m | 31% | 5.0 m | 50% |
| Top endcap 1 | 3.7 m | 27% | 3.9 m | 30% |
| Top endcap 2 | 3.6 m | 24% | 4.3 m | 37% |
| Bottom endcap 1 | 3.6 m | 24% | 4.3 m | 37% |
| Bottom endcap 2 | 3.5 m | 22% | 6.1 m | 66% |

Table III: Results for PMT saturation using the diffuser configuration detailed in Table I with 5.5 M photons per pulse.

| OD location | Diffuser position (cm) | Mean charge (pe) at sat. distance | Mean charge (pe) at sat. limit $\pm 2\sigma$ |
|-----------------|--------------------------|-----------------------------------|----------------------------------------------|
| Barrel 1 | (395.65,-3281.50,8.75) | 108 | 68 ± 12 |
| Barrel 2 | (3281.50,395.65,1705.55) | 105 | 67 ± 11 |
| Top endcap 1 | (-70.7,-97.3,3350.82) | 106 | 96 ± 14 |
| Top endcap 2 | (-707,-968.2,3350.82) | 108 | 77 ± 13 |
| Bottom endcap 1 | (-707,-968.2,-3350.82) | 108 | 77 ± 14 |
| Bottom endcap 2 | (707,-1157.8,-3350.82) | 114 | 42 ± 11 |

Table IV: PMT saturation levels for the figures of merit detailed in Table III with 5.5 M photons per pulse.

| OD location | Mean saturation distance | % PMTs within saturation distance | Saturation limit | % PMTs within saturation limit |
|-----------------|--------------------------|-----------------------------------|------------------|--------------------------------|
| Barrel 1 | 5.4 m | 57% | 6.9 m | 86% |
| Barrel 2 | 5.4 m | 57% | 6.9 m | 86% |
| Top endcap 1 | 5.3 m | 48% | 6.3 m | 69% |
| Top endcap 2 | 4.3 m | 37% | 6.7 m | 74% |
| Bottom endcap 1 | 4.3 m | 37% | 6.4 m | 70% |
| Bottom endcap 2 | 4.3 m | 37% | 6.5 m | 72% |

Table V: Results for PMT saturation using the diffuser configuration detailed in Table I with 10 M photons per pulse.

| OD location | Diffuser position (cm) | Mean charge (pe) at sat. distance | Mean charge (pe) at sat. limit $\pm 2\sigma$ |
|-----------------|--------------------------|-----------------------------------|----------------------------------------------|
| Barrel 1 | (395.65,-3281.50,8.75) | 102 | 70 ± 12 |
| Barrel 2 | (3281.50,395.65,1705.55) | 104 | 69 ± 12 |
| Top endcap 1 | (-70.7,-97.3,3350.82) | 102 | 72 ± 15 |
| Top endcap 2 | (-707,-968.2,3350.82) | 139 | 65 ± 13 |
| Bottom endcap 1 | (-707,-968.2,-3350.82) | 142 | 70 ± 12 |
| Bottom endcap 2 | (707,-1157.8,-3350.82) | 141 | 69 ± 11 |

Table VI: PMT saturation levels for the figures of merit detailed in Table III with 10 M photons per pulse.

²³² barrel is higher than in the endcaps (with the exception of the bottom endcap 2 diffuser with
²³³ 5.5 M photons per pulse) with 86% of barrel PMTs within the saturation limit of 6.9 m. It
²³⁴ should be noted that changes to the OD geometry, including the addition of PMTs in the

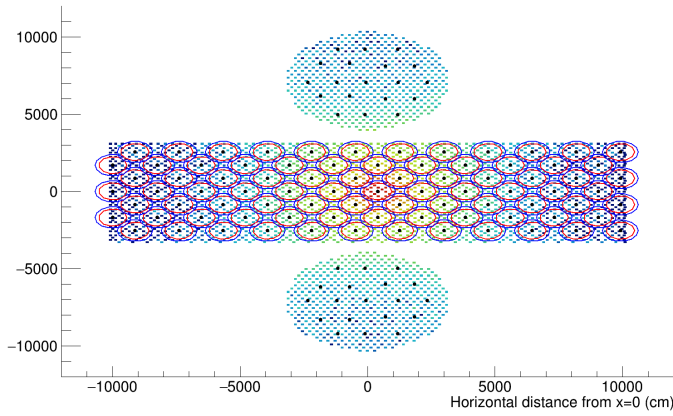


Figure 5: Charge in pe on each PMT as a result of illumination with the barrel 1 diffuser illuminated by 10 M photons per pulse. The mean saturation distance and saturation limit around each PMT in the barrel are marked in red (smaller circles) and blue (larger circles) respectively.

235 endcaps, are possible, and have not been taken into account in this simulation.

236 The diffuser position with respect to the surrounding PMTs has an observable effect
 237 on the saturation levels achieved. Where the diffuser positions with respect to surrounding
 238 PMTs are equivalent, as in the case of the two barrel diffusers, as well as the bottom endcap
 239 1 and top endcap 2 diffusers, saturation levels are largely the same for both light intensities.
 240 However, the positions of the top endcap 1 and bottom endcap 2 diffuser each differ from
 241 all other diffusers simulated, resulting in different saturation distances and saturation lim-
 242 its. Again, a full simulation of all diffuser positions should be carried out to fully evaluate
 243 achievable saturation across the whole detector, once all parameters and geometries have
 244 been finalised.

245 4 OD Collimator Studies

246 Collimated light sources will be used to make measurements of scattering and absorption in
 247 water, and Tyvek reflectivity. These will be used to calibrate for changes in the detector
 248 properties over time. This will require untangling the effect of each of the properties in order
 249 to discriminate changes in each of the properties. The first step is to evaluate the sensitivity
 250 of collimators to changes in each of the properties separately.

251 This section presents the collimator sensitivity studies which were carried out in 2023,
 252 prior to updates to the OD geometry and more recent updates to the light-injector simulation.
 253 Section 4.1 describes the positioning of collimators, and the simulation method. The analysis
 254 of sensitivity to water properties and Tyvek reflectivity are presented in Section 4.2, and the
 255 results are presented in Section 4.3.

256 4.1 Collimator Simulation

257 The collimated light sources were simulated using the LI simulation described in Section 3.1.
 258 For this collimator study, a flat profile with an opening angle of 2° was taken as the baseline,
 259 and the OD configuration described in Table II in Section 3.2 was used. Figure 6 shows the
 260 charge map produced by the 2° collimator source in the top endcap.

261 The sensitivity of each of the collimators to changes in absorption, Rayleigh scattering

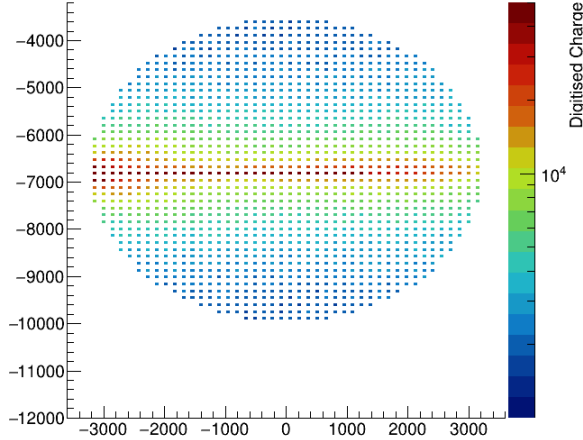


Figure 6: Distribution of charge collected in end cap PMTs for a collimated beam of light injected from the right hand side, travelling across the diameter of the OD to the left hand side.

and Tyvek reflectivity was evaluated by varying each property one at a time, scanning over values up to 30% either side of the nominal value for absorption and scattering, and 30% lower than the expected value for Tyvek reflectivity. Nominal values have been extrapolated from Super-Kamiokande measured values in the case of scattering and absorption, and from the expected value in the case of the Tyvek reflectivity. These values and the range of the scans over each property are shown in Figure 7.

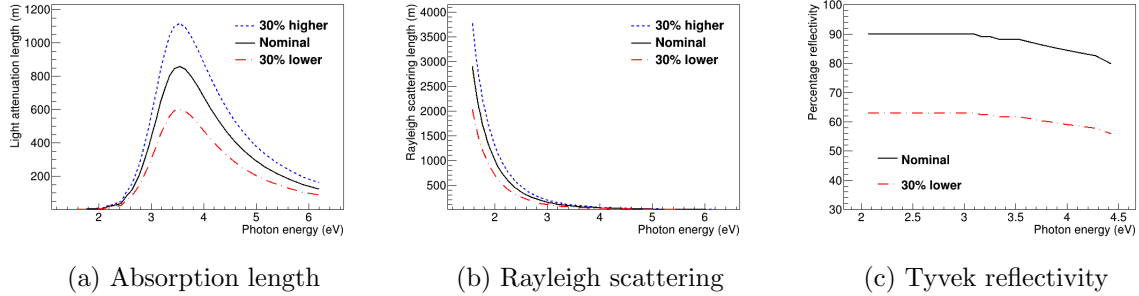


Figure 7: Nominal (black, solid), maximum (blue, dashed) and minimum (red, dot-dashed) values for the scans over absorption length and Rayleigh scattering, and nominal (black, solid) and minimum (red, dot-dashed) values for the scans over Tyvek reflectivity.

Variable steps were chosen for the scan over the range for each property to allow sufficiently detailed evaluation of the sensitivity to changes in each property. For absorption and scattering, the parameters are varied in steps of 1% between $\pm 5\%$, where finer binning is required to see the small effects at these variations. From 5% to 30% either side of the nominal, the parameters were varied in 5% steps. For Tyvek reflectivity, the parameter is reduced by up to 30% either side of the nominal, in 0.5% steps up to $\pm 5\%$, 1% steps between $\pm 5\%$ and $\pm 10\%$ and in 5% steps above that.

The scans over the variation in parameters require at least 21 individual simulations per property, and each simulation requires $\mathcal{O}(100M)$ photons to produce sufficient statistics. In addition, the OD geometry remains in flux. As such, although the OD light injection system will include 12 OD collimators, a single collimator in each of the OD top endcap, barrel and

279 bottom endcap was simulated for the purposes of these studies.

280 4.2 Collimator Sensitivity Analysis

To evaluate the sensitivity of the collimator to each of the parameters, the distribution of charged collected in the PMTs as a function of the distance from the light injector was compared over the scan ranges detailed in Section 4.1. These were compared using a Pearson's χ^2 test:

$$281 \quad \chi^2 = \sum_{s=0}^S \frac{(O_s - E_s)^2}{E_s}, \quad (1)$$

281 where the expected value E_s is the charge on the PMTs at distance s for the nominal
282 parameter value, and the observed value O_s is the charge on the PMTs at distance s for
283 the varied parameter value. In this way, the distribution of χ^2 values as a function of
284 the percentage change in parameter value indicates the sensitivity of the collimator to the
285 changes in each of the properties. For this analysis, only PMTs located in the same part of
286 the detector as the collimator were included in the χ^2 calculation.

287 Errors on the χ^2 statistic were calculated by splitting the sample into 10 sub-samples,
288 calculating the Pearson's χ^2 test statistic for each sub-sample and then calculating a relative
289 standard deviation from the variance between the sub-samples.

290 4.3 Results

291 Figure 8 shows the χ^2/ndof values over the scan ranges for each of the properties investigated
292 for a 2° collimator located at the bottom of the OD and pointing upwards in the OD barrel.
293 The collimator is most sensitive to changes in reflectivity, and least sensitive to changes in
294 absorption.

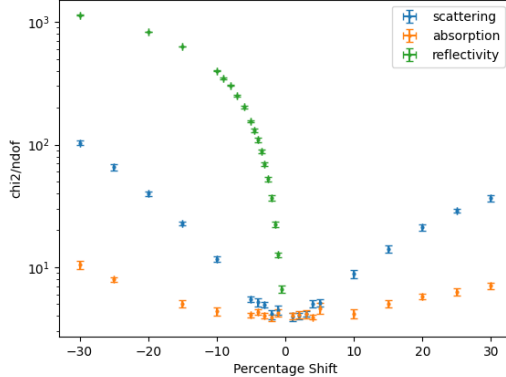


Figure 8: Change in χ^2 statistic with variation in absorption (orange), Rayleigh scattering (blue) and Tyvek reflectivity (green) up to 30% from the nominal value.

295 For the baseline analysis, the collimator has been positioned close to the front face of
296 the PMTs. However, the location of the collimator, in terms of distance from the front face
297 of the PMTs, can affect the sensitivity to changes in the parameters, particularly in the
298 case of reflectivity, as shown in Figure 9. Ultimately the positioning of the collimator will
299 be constrained by practical considerations and, as such, the sensitivity of the collimators
300 to absorption, scattering and Tyvek reflectivity should be reassessed once the OD geometry
301 and collimator positioning have been finalised.

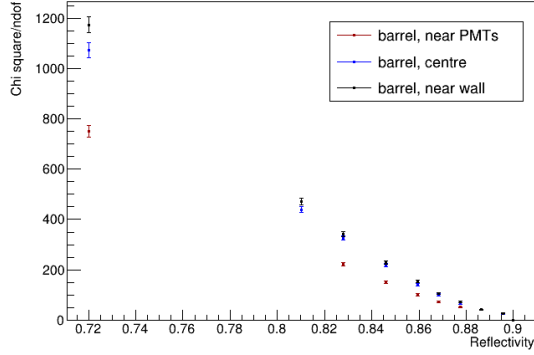


Figure 9: Change in χ^2 statistic with variation in Tyvek reflectivity up to 30% from the nominal value for a collimator positioned close to the PMTs (red), halfway between the PMTs and tank wall (blue), and close to the tank wall (black).

302 The collimators have been designed to be tunable to different open angles. A comparison
 303 of the results for a 2° and 1.35° collimator in the same position in the barrel is shown in Fig-
 304 ure 10. With a straight comparison of the Pearson's χ^2 test statistic for the two collimators,
 305 there was no obvious change in the sensitivity to changes in any of the parameters. However,
 306 a more detailed analysis which takes into account additional information, such as the timing
 307 of the PMT hits as a function of PMT location, should be performed to re-evaluate the effect
 308 of the opening angle on collimator sensitivity to each of the properties investigated.

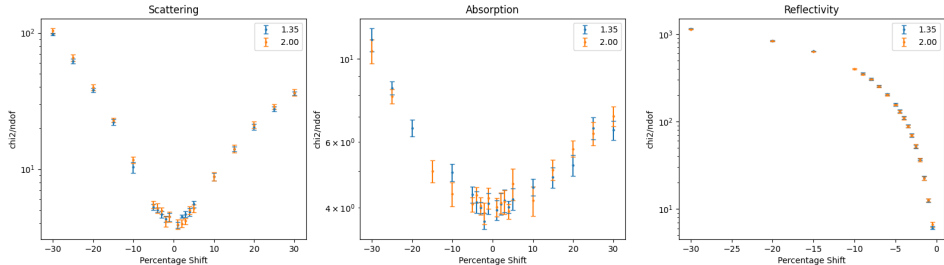


Figure 10: Change in χ^2 statistic with variation in Rayleigh scattering (left), absorption (centre) and Tyvek reflectivity (right) up to 30% from the nominal value for a 2° collimator (orange) and 1.35° collimator (blue).

309 These results represent a preliminary evaluation of the sensitivity of the OD collimator
 310 system to the three properties investigated, and presents the first step in the development
 311 of an analysis to measure these properties using the collimator system. This will rely on
 312 discriminating the effect of changes in each property simultaneously and will require a more
 313 complex analysis. This analysis should be performed once the OD geometry has been fi-
 314 nalised.

315 **5 Diffuser Design**

316 **5.1 ID Diffuser Hemisphere Design**

317 **5.1.1 Inner Detector Diffuser Design**

318 The diffusers used to scatter input laser light in the inner detector volume are 2.54 cm
319 half-spheres fabricated from PTFE. This is used as it

- 320 • is unaffected by immersion in water
321 • acts as a excellent diffuser
322 • is a good transmitter of UV light
323 • is easy to machine and clean

324 A mechanical drawing of the inner detector diffuser hemispheres is shown in Figure 11

325 **5.1.2 Diffuser Profile Measurement System**

326 A scanning system was built to measure the output characteristics of diffuser hemispheres.
327 Enclosed in a dark box, the diffuser is mounted onto two rotary stages which gives the freedom
328 to rotate the diffuser around the nominal axis linking the diffuser with the photosensor. This
329 scanner only takes scans in an air medium, and the setup is illustrated in Figure 12.

330 A laser powered from a wall plug is used to illuminate the diffuser with light at a wave-
331 length of 450 nm. It is triggered by a function generator with 1000 triggers per burst at a
332 frequency of 2 kHz. The open beam is directed via a mirror, a circulator, and a lens to the
333 fibre launch stage, and then via an optical fibre towards the diffuser. The diffuser enclosure is
334 fixed with three screws on the double-rotation stage. Measurements of bare diffuser profiles,
335 i.e. without enclosure, are conducted with the bare fibre end positioned in the centre of the
336 rotation stage using a 3D printed frame. The bare fibre end is kept in place due to friction
337 on the connection point with the diffuser hemisphere. A photograph of the rotation stage
338 with a bare diffuser hemisphere is shown in Figure 13.

339 A PMT measures the diffuser spectrum at a fixed position, with 62 cm distance to the
340 diffuser enclosure and a 3 mm pinhole aperture, restricting the solid angle viewed by the PMT
341 to $2 \cdot 10^{-5}$ sr. For comparison, a single 50 cm PMT in the HK far detector receives light from
342 a point source at the other side of the tank over a solid angle of approximately $2.2 \cdot 10^{-4}$ sr.
343 The PMT signal is digitised at a sampling rate of 2500 MHz over 1000 cycles, allowing to
344 resolve the shape of each single signal waveform. The light yield at each coordinate is then
345 obtained as the average waveform area across all digitised signals.

346 The diffuser profile measurement system is discussed in detail in [5].

347 **5.1.3 Diffuser Power Measurement System**

348 In addition to the profile measurement functionality, the integrated power output from the
349 diffuser was measured using an integrating sphere from Ophir. This sphere provides an
350 unbiased measurement of the total light output power of any light source, regardless of the
351 shape of the emission profile. A bespoke diffuser holder suitable for connection to one of the
352 integrating sphere ports was 3D-printed, as was a holder for the optical fibre from the laser
353 source.

354 A bare PTFE hemisphere was mounted into this holder and connected into the integrating
355 sphere port. The bare end is inserted into the connection point in the same manner as for
356 a bare profile scan. Tape was used to in order to prevent light leaking out of the back

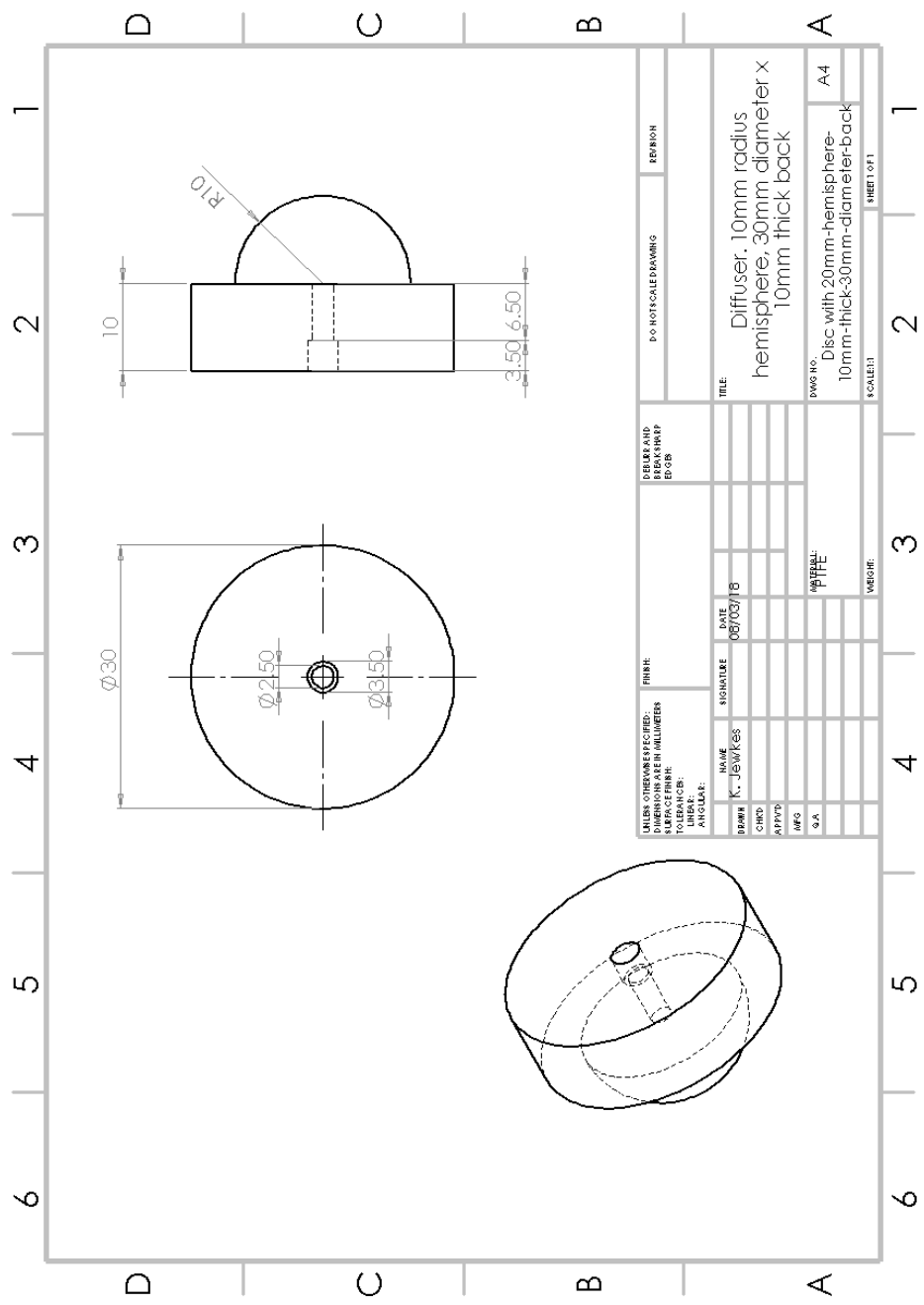


Figure 11: Bare Diffuser Mechanical Drawing

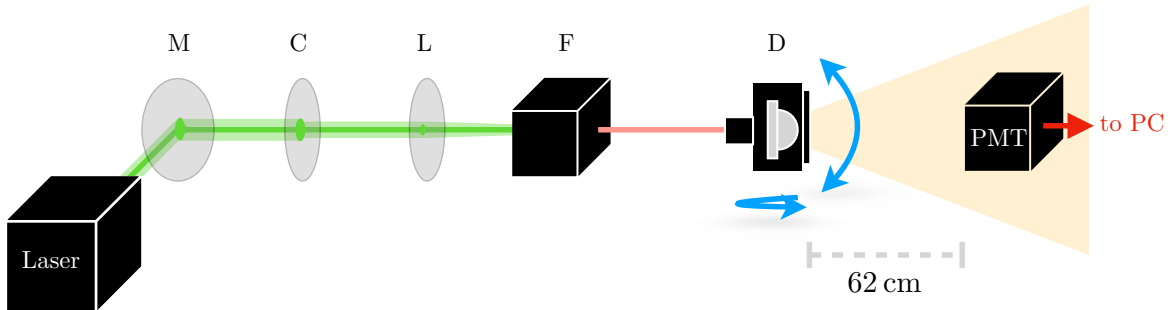


Figure 12: Setup for diffuser scans: light from the laser is directed via a mirror (M), a circulator (C), and a lens (L) to the fibre launch stage (F). From there, the light goes via an optical fibre to the diffuser (D) on the rotation stage.

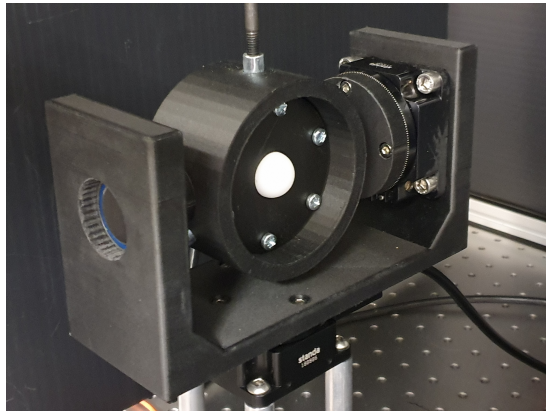


Figure 13: Rotation stage with bare diffuser hemisphere mounted using a 3D-printed frame.

of the hemisphere during the measurement, which also helped to keep the fibre in place. The hemisphere was then illuminated with light from the same laser, this time running on a continuous rather than burst setting. On the continuous setting light is supplied in a sinusoidal manner at a frequency of 1 kHz. Power measurements were taken once per second for a period of ten seconds to account for small fluctuations in laser intensity, the mean of which served as the final power measurement for that hemisphere.

In order to calculate a power ratio, a measurement of power for the bare fibre also needed to be obtained. This was done in a similar manner to a power measurement for a hemisphere, using the same laser and data acquisition settings. To make the comparison between fibre and hemisphere measurement as accurate as possible, a special hemisphere was created with the fibre connection point extended into a hole that runs through the length of the hemisphere. The bare fibre can then be inserted all the way through until it pokes out of the front, allowing a power measurement for the bare fibre to be taken with the conditions inside the integrating sphere as close as possible to hemisphere measurements. The ratio of hemisphere power to fibre power can then be taken to determine the amount of light lost.

A table of systematics for the power ratio measurement is shown in Table VII. Rotation refers to changing the orientation at which the diffuser is placed into the holder, and diffuser re-insertion refers to removing the diffuser from the holder and replacing it. Fibre re-insertions refers to disconnecting and re-connecting the fibre into the diffuser, while bare fibre refers to dis- and re-connecting the fibre when taking bare fibre measurements. This results in a total systematic of 5.3% for a diffuser measurement and 1.8% for a fibre measurement, and therefore an uncertainty of 5.6% in a power ratio measurement.

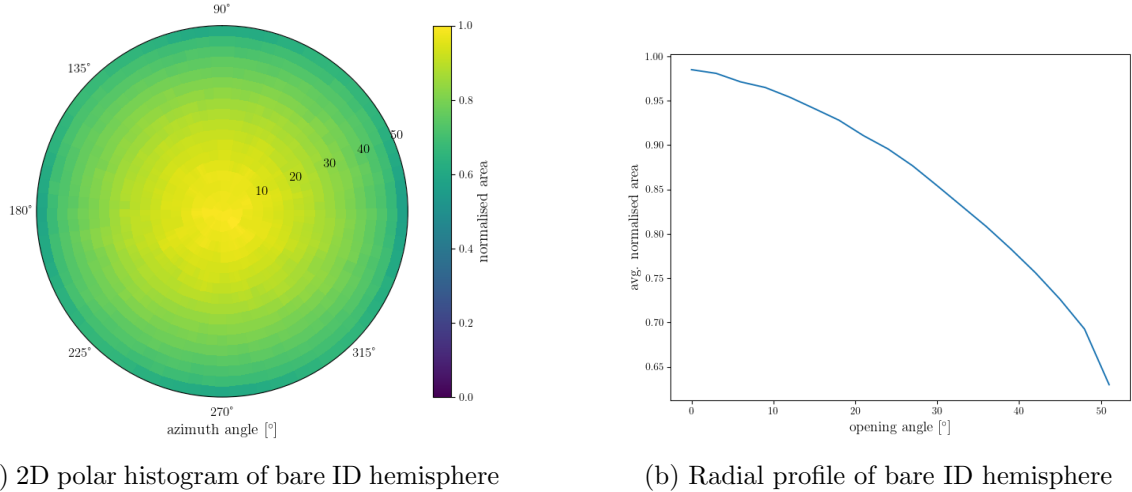


Figure 14: Profile scan of a standard bare ID diffuser hemisphere

| Systematic | Std. dev. (%) |
|-------------------------|---------------|
| Rotation | 1.4 |
| Diffuser re-insertion | 1.0 |
| Fibre re-insertion | 5.0 |
| Bare fibre re-insertion | 1.8 |

Table VII: Integrating sphere systematics for the power ratio measurement.

379 5.2 OD Diffuser Design

380 The original intention was to use the same diffuser hemisphere design for the OD diffusers
 381 as will be used for the ID diffusers. However, the standard diffuser emits less than 20% of
 382 the power delivered by an optical fibre. As there are a number of interfaces in the optical
 383 pathway between the light source and the diffuser, and as the light source for the OD will
 384 be LEDs, this was considered too low to be able to effectively saturate PMTs in the OD
 385 space, which is one of the primary design requirements of the system. Neither the number of
 386 interfaces in the optical chain, nor the light source can be changed easily, but it is possible
 387 that an alternate design of the diffuser hemisphere could yield more light.

388 Light is lost to two mechanisms in the standard diffuser; absorption by the PTFE and



Figure 15: A prototype of the OD diffuser with a 2 mm top hat.

389 backscattering. Both loss mechanisms would be minimised if there were less PTFE in the
 390 light path. The design for the OD diffuser section was modified to be the shape of a top
 391 hat, as shown in Figure 15. The optimal depth was studied by taking profile and power
 392 ratio measurements using the same diffuser, but at smaller and smaller depths; after each
 393 measurement was completed, 2.0 mm was cut from the top-hat, and the measurements were
 394 re-taken. This procedure was repeated until the top-hat was 2.0 mm high.

| Top-hat depth (mm) | Power ratio (%) |
|--------------------|-----------------|
| 10.0 | 19.2 |
| 8.0 | 32.4 |
| 6.0 | 31.5 |
| 4.0 | 42.1 |
| 2.0 | 55.2 |

Table VIII: Power ratio measurements for each depth of the top-hat

395 Results of the power ratio measurements are shown in Table VIII. As expected, power
 396 ratio increases with decreasing top-hat depth, making the optimum depth 2.0 mm. The
 397 profile as shown in Figure 16 confirms that the shape of the profile is still suitable.

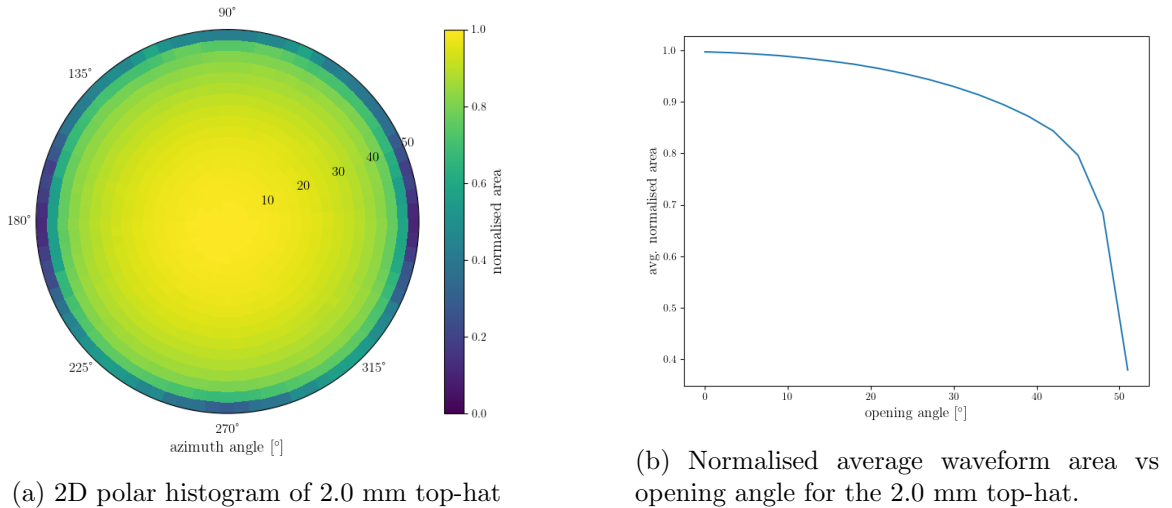


Figure 16: Profile scan of the 2.0 mm top-hat

398 Based on these studies, we propose to change the OD diffuser design from a hemisphere
 399 to a top-hat with a 2.0 mm height above the base. The diffuser will still be fabricated from
 400 PTFE, but this new design (i) emits more light at higher emission angles (ii) doubles the
 401 amount of light that is emitted for a given LED power setting and (iii) is significantly easier
 402 to fabricate in bulk.

403 6 OD Diffuser Mounting System and Installation

404 The OD space will be illuminated by a total of 122 OD diffusers, 19 on each of the top and
 405 bottom caps, and 84 in the barrel. The barrel diffusers are distributed in 7 vertical layers
 406 each consisting of 12 OD diffusers. Due to the numbers and cost, the mounting system must
 407 be relatively small, easy to fabricate and easy to install. Installation will be carried out by
 408 workers on the gondola in the OD space after the Tyvek has been installed and as the fibres
 409 are being installed. The gondola worker will install the fibre in the OD diffuser, and fix the



Figure 17: (left) Front view of the prototype of the OD diffuser mount and (right) rear view of the prototype of the OD diffuser mount.

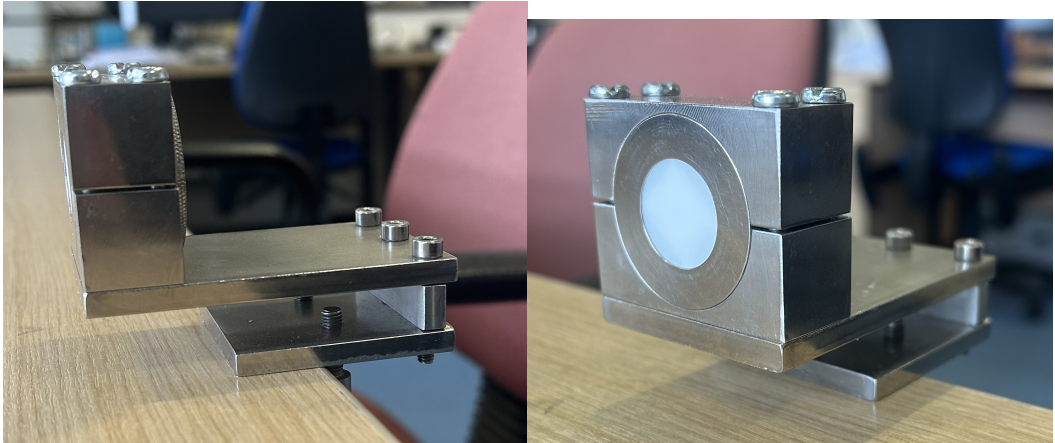


Figure 18: (left) Side view of the prototype holder and (right) front view of the prototype holder.

410 mount to the HK frame, oriented into the OD space. Since this is being done on the gondola,
411 the mount needs to be small, easy to store, and straightforward to install.

412 Drawings for the OD diffuser prototype mount can be seen in Figure 17 and pictures
413 of the prototype can be seen in Figure 18. The mount is made from stainless steel and is
414 designed to hook over a horizontal frame bar, and screw in from the bottom. The PTFE
415 mount is approximately 5 cm on a side. The fibre will be installed from the back and is held
416 in place by a T-shaped component that is screwed down by the gondola worker. An image of
417 the prototype housing installed on the PMT support structure mockup next to a mechanical
418 OD PMT and WLS plate is given in Figure 19.

419 7 Pulser Board

420 7.1 Pulser Board Overview

421 The pulser board was designed to be a more efficient and compact version compared to
422 Super-Kamiokande UK Light Injection system, improving on efficiency, functionality, and
423 light output. The pulser board is a rather simple board designed for low cost production.
424 This section explains each circuit, component selection and design decision. Minor changes
425 are expected from the current design, mostly centred on removing prototyping circuitry.
426 More details on the expected changes are given in Section 7.10.



Figure 19: OD diffuser housing installed at the RAL mockup frame, next to an OD PMT and WLS plate.

427 7.2 Physical Dimensions and Construction

428 The dimensions of the Printed Circuit Board (PCB) were selected to be as compact as practicable, while still providing sufficient area for the secure mounting of a fibre coupler and for
 429 the components. The final board size is 50 mm × 30 mm. This configuration permits electrically noisy components, such as switching power supplies and the Low Voltage Differential
 430 Signal to Transistor Transistor Logic (LVDS-to-TTL) converter to be positioned at a maximum
 431 distance from the switching circuitry, thereby minimising potential electromagnetic
 432 interference.
 433

434 Although it is technically feasible to further reduce the board size, preliminary design
 435 studies and practical build indicated no substantial benefit in doing so. The board density
 436 cannot be significantly increased inside the crate due to FPGA LVDS count and Eurocard
 437 dimension, and cost analyses revealed negligible differences associated with a smaller PCB
 438 footprint. Furthermore, the chosen dimensions provide an adequate area for the fibre coupler
 439 and the necessary mounting holes to affix the pulser board onto the Eurocard, thereby
 440 ensuring reliable optical alignment and mechanical stability. The PCB is fabricated as a four-
 441 layer FR4 [6] board with a thickness of 0.8 mm, in accordance with the standard construction
 442 offered by PCB Train/Newbury Electronics¹, see Figure 20. Refer to Figure 21 for the 3D
 443 model of the pulser board. The Top Layer and Inner Top Layer are shown in Figure 22, and
 444 the Inner Bottom Layer and Bottom Layer are likewise illustrated in Figure 23. A combined
 445 view of all PCB layers is provided in Figure 24.

446 ¹These are trading names of the same manufacturer.

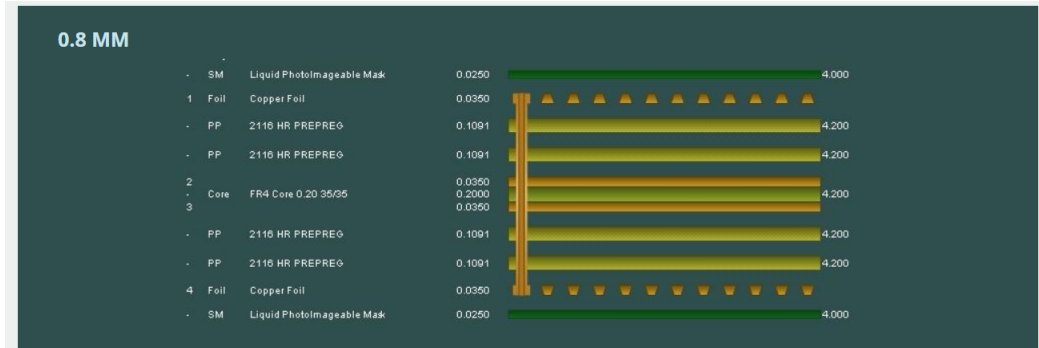


Figure 20: PCB Train's 4 Layer 0.8mm Layer Stack

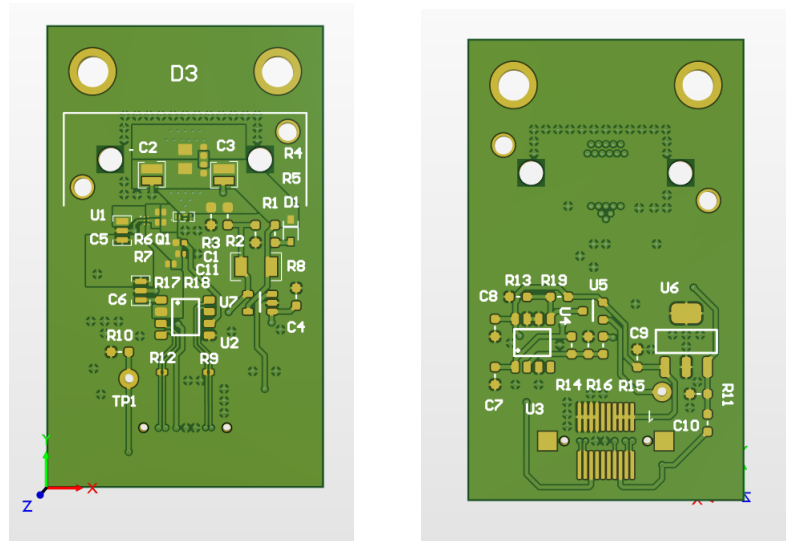


Figure 21: Pulser Board's 3D view Top and Bottom

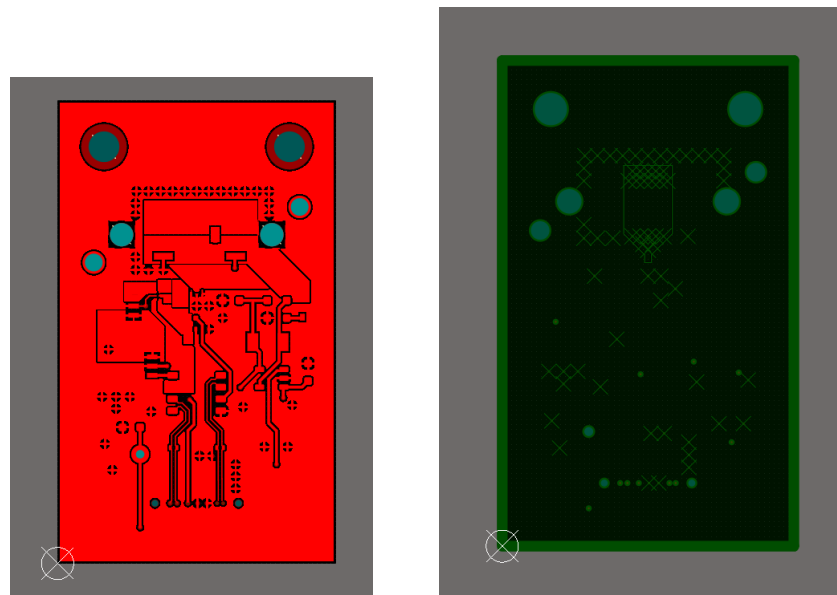


Figure 22: Pulser Board Top and Inner Top Layer

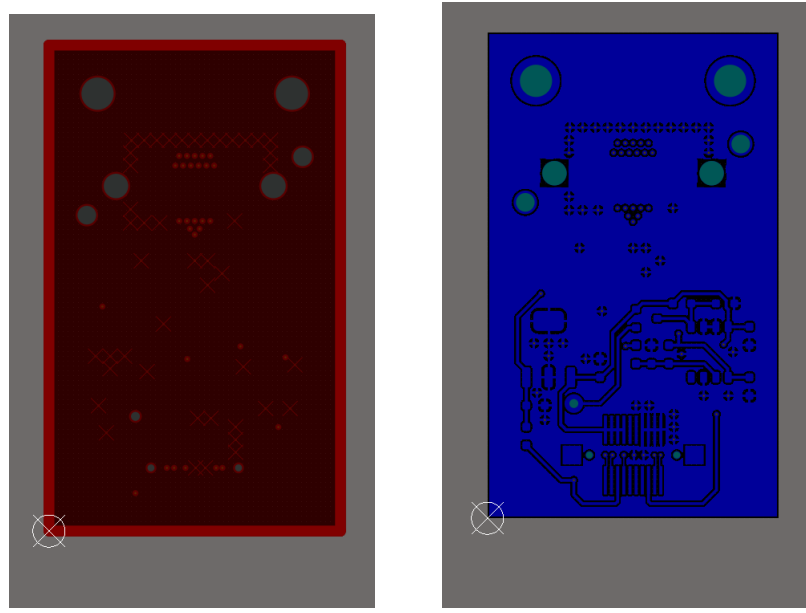


Figure 23: Pulser Board Inner Bottom and Bottom Layer

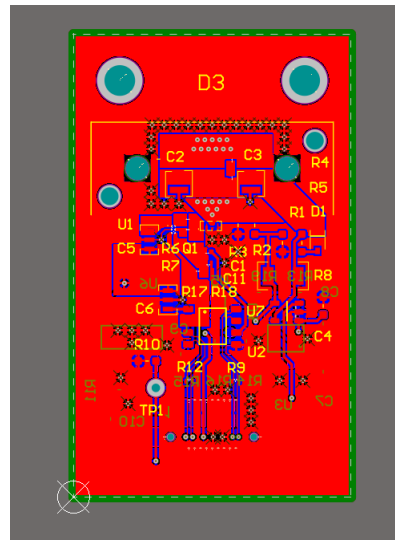


Figure 24: Pulser Board Layer Overview

447 **7.3 LED**

448 **7.3.1 Overview**

449 The LEDs are the most crucial component in the system as the characteristics of these
 450 primarily determine the light output, regardless of electronics. LEDs are usually not rated
 451 for such high-speed applications, which meant LEDs had to be tested and validated in-house,
 452 as datasheets do not provide the required information. The specification required was a 1–
 453 10 ns clean single pulse, sub-400 nm wavelength, small surface mount package, narrow output
 454 beam so it can be coupled to a fibre with reduced losses and a good range of photon output.
 455 Several LED packages were purchased from Kingbright and LC-LED, and their performance
 456 tested. The results of these tests are given in Section 7.3.4.

457 **7.3.2 Switching Circuit**

458 The redesign process provided a valuable opportunity to evaluate a revised layout and new
 459 components for the switching circuit. Several enhancements have since been implemented
 460 in the revised switching circuit. Most importantly, the switching side of the layout has
 461 been rerouted. In contrast to the previous configuration, where current would flow through
 462 the limiting resistor regardless of the LED state, the updated design only allows current
 463 flow when the LED is active (refer to Figure 25). This modification reduces both thermal
 464 dissipation and the overall power consumption of the system. To modulate light intensity,
 465 a variable power supply is now employed to adjust the voltage supplied to the LED. This
 466 method has proven highly effective. Tests were conducted at various voltage levels using
 467 the full 181 m length of optical fibre—the maximum expected in Hyper-K at the time of
 468 testing—and the resulting photon output ranged from approximately 1×10^5 to 2×10^7
 469 photons per pulse. Refined testing results are shown in Section 7.3.4. Further discussion
 470 regarding the implementation and performance of the variable voltage supply is provided in
 471 Section 7.5.

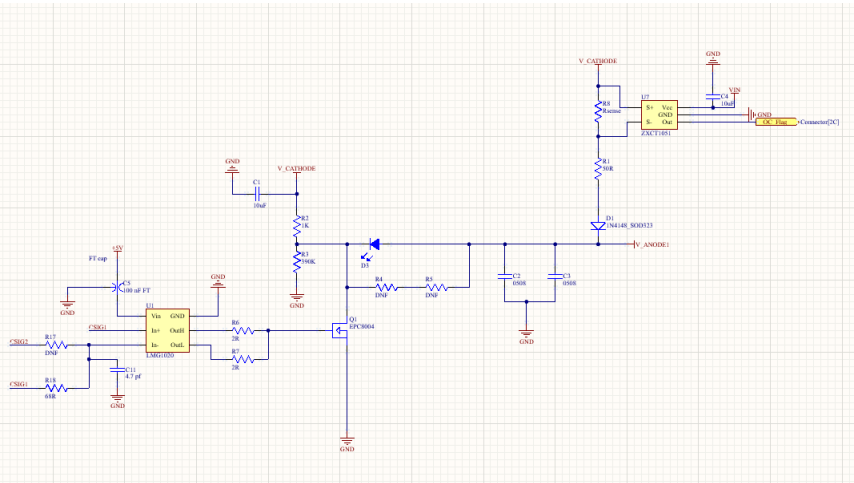


Figure 25: Switching Circuit Layout with LMG1020 and over current IC, R4 is 6.8 nH inductor and R5 is 3R3 resistor

472 **7.3.3 Switch Selection**

473 The previous iteration of the pulser board utilised a BFR92 [7] high-speed RF NPN switching
 474 transistor which was directly driven by a LVDS-to-TTL converter. In the redesign phase,

475 alternative circuit topologies were explored—particularly those suitable for generating (sub-
476)nanosecond pulses. This investigation led to the adoption of gate driver circuits. Gate
477 drivers are advantageous not only because they can power switches with challenging drive
478 requirements, but also because sub-nanosecond electrical pulses can be achieved by modu-
479 lating the enable pin with slight timing offsets.

480 The fastest commercially available gate driver identified was the Texas Instruments
481 LMG1020 [8]. This device supports pulse widths down to 1 ns, with typical rise and fall
482 times of 400 ps. Additionally, it features an enable pin that allows for precise nanosecond
483 pulse shaping ². The LMG1020 is compatible with both Gallium Nitride Field Effect Tran-
484 sistor (GaN) and Metal Oxide Semiconductor Field Effect Transistor (MOSFET) switches,
485 broadening the scope for future component integration and experimentation. It is widely
486 available and priced at £1.97 per unit in the quantities we will require for full production.

487 For the switching element, enhancement-mode GaN transistors manufactured by EPC
488 were selected due to their superior switching characteristics. This recommendation origi-
489 nated from Nick Braam, an engineer at the University of Victoria, who contributed to the
490 pulser board design for the mPMT system [9]. Two EPC devices were shortlisted: the
491 EPC2012 [10] and EPC8004 [11]. The EPC2012 offers a simpler footprint, which could re-
492 duce manufacturing defects. However, the EPC8004 features lower parasitic capacitance,
493 see Figure 26 for the EPC2012 values and Figure 27 for EPC8004 values, leading to better
494 high-speed performance.

495 To evaluate optical output performance, a 40 m length of FP400URT [2] optical fibre,
496 a Mouser-sourced 385 nm LED (ATS2012UV385 [12]), and a Hamamatsu H10721-210 [13]
497 PMT were used. The EPC-based configurations exhibited nearly identical pulse shapes,
498 whereas the BFR92-based circuit’s pulse shape was less sharp at identical pulse widths, as
499 shown in Figure 28. Consequently, the EPC8004 (Figure 29) was chosen for implementation.
500 Optimal performance of the EPC GaN switches required careful layout considerations. A
501 layout was developed in accordance with EPC’s design guidelines [14], targeting minimal
502 parasitic inductance and capacitance. The design employs two layers placed directly above
503 one another, utilising large copper planes and multiple vias to ensure uniform current dis-
504 tribution. The PCB will be fabricated and assembled by PCB Train, using their 0.8 mm
505 thick, four-layer stack-up, which offers minimal inter-layer separation for optimal electrical
506 performance (Figure 20). This same layout strategy was applied to the BFR92 circuit to
507 provide a fair performance comparison.

508 A significant challenge at low pulse widths is the presence of a trailing edge or “tail” in
509 the LED output. This effect arises due to charge accumulation and the intrinsic capacitance
510 of the LED, resulting in extended decay times and pulse broadening (see Figure 30). To
511 mitigate this, a parallel modified snubber circuit was implemented, consisting of a 6.8 nH
512 inductor and a 3.3 Ω current-limiting resistor. Upon LED turn-off, the inductor generates an
513 electromotive force (EMF) that actively extracts residual charge from the LED, accelerating
514 its shutdown. The effectiveness of this approach is illustrated in Figure 31. Additionally,
515 two 0508 reverse-topology 100 nF capacitors have been incorporated. Their role is to act as
516 local energy reservoirs, providing rapid current delivery to the LED during pulse operation,
517 surpassing the response time of the main power supply.

518 7.3.4 Testing

519 For testing purposes, the previous-generation United Kingdom Light Injection (UKLI) moth-
520 erboard and associated software were utilised in conjunction with a prototype of the next-
521 generation pulser board. This prototype consisted of four distinct circuit variants: one

²See page 12 and 13 in [8].

| PARAMETER | TEST CONDITIONS | MIN | TYP | MAX | UNIT |
|------------------------------------------------------------------------------------|------------------------------------------------------------|-----|-----|-----|------|
| Dynamic Characteristics ($T_j = 25^\circ\text{C}$ unless otherwise stated) | | | | | |
| C_{ISS} | $V_{\text{DS}} = 100\text{ V}, V_{\text{GS}} = 0\text{ V}$ | | 128 | 145 | pF |
| C_{OSS} | | | 73 | 95 | |
| C_{RSS} | | | 3.3 | 4.4 | |

Figure 26: EPC2012 Capacitance Values IC

| PARAMETER | TEST CONDITIONS | MIN | TYP | MAX | UNIT |
|------------------------------------------------------------------------------------------------|-----------------------------------------------------------|-----|-----|-----|------|
| Dynamic Characteristics[#] ($T_j = 25^\circ\text{C}$ unless otherwise stated) | | | | | |
| C_{ISS} | $V_{\text{GS}} = 0\text{ V}, V_{\text{DS}} = 20\text{ V}$ | | 45 | 52 | pF |
| C_{OSS} | | | 23 | 34 | |
| C_{RSS} | | | 0.8 | 1.3 | |

Figure 27: EPC8004 Capacitance Values IC

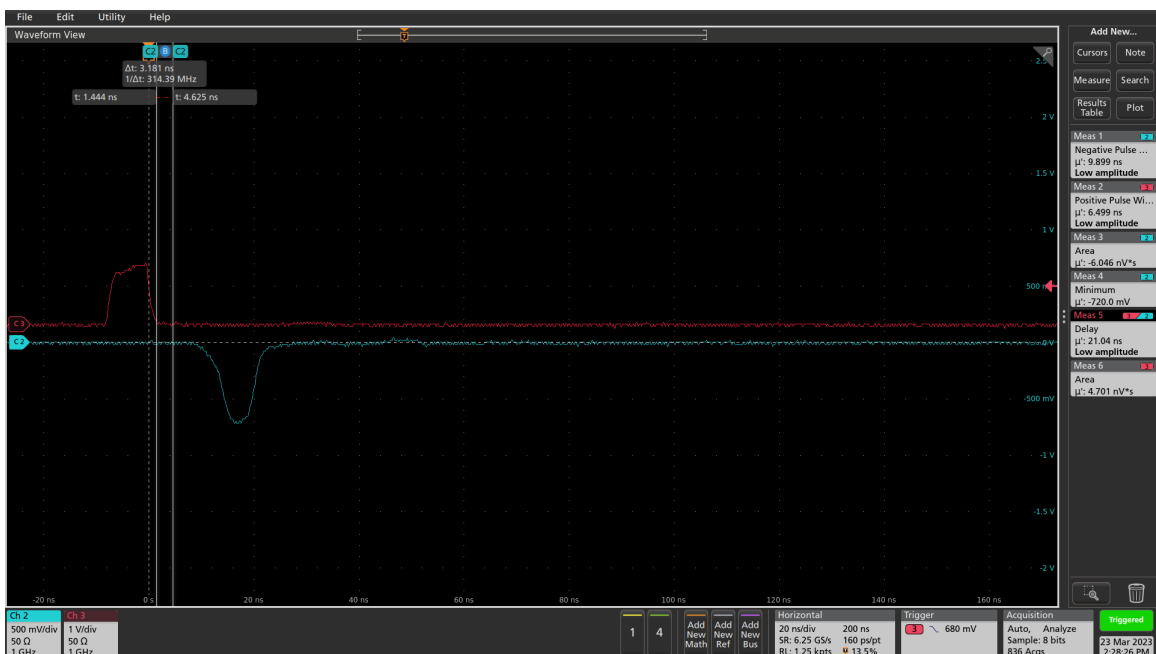


Figure 28: BFR92 Pulse Shape

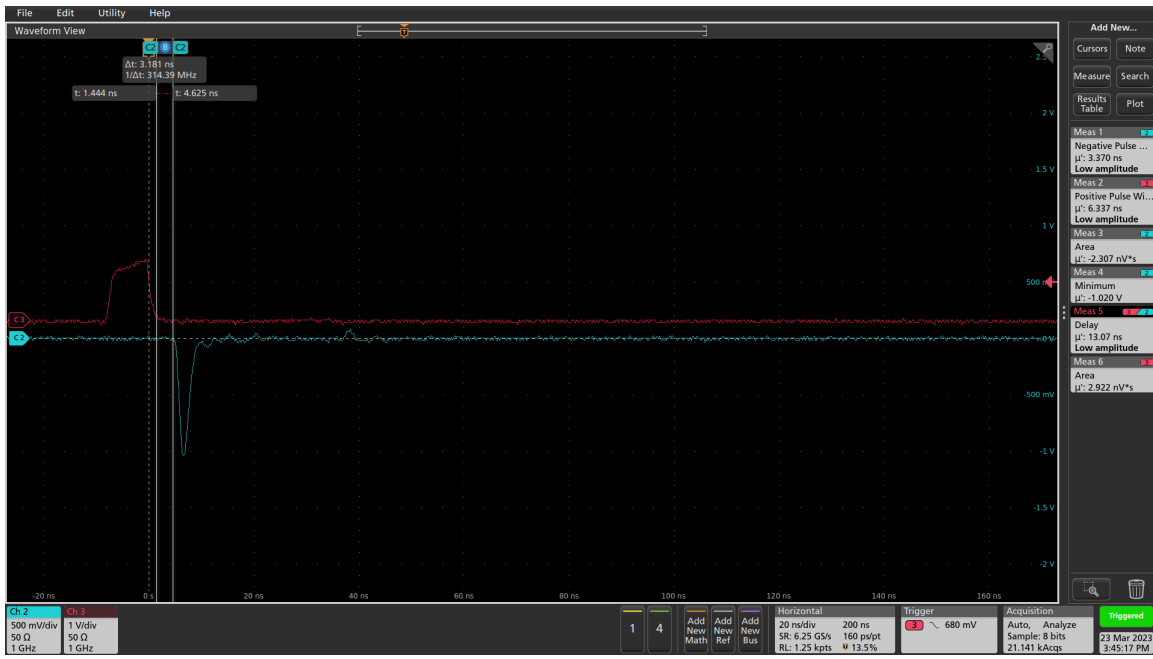


Figure 29: EPC8004 Pulse Shape

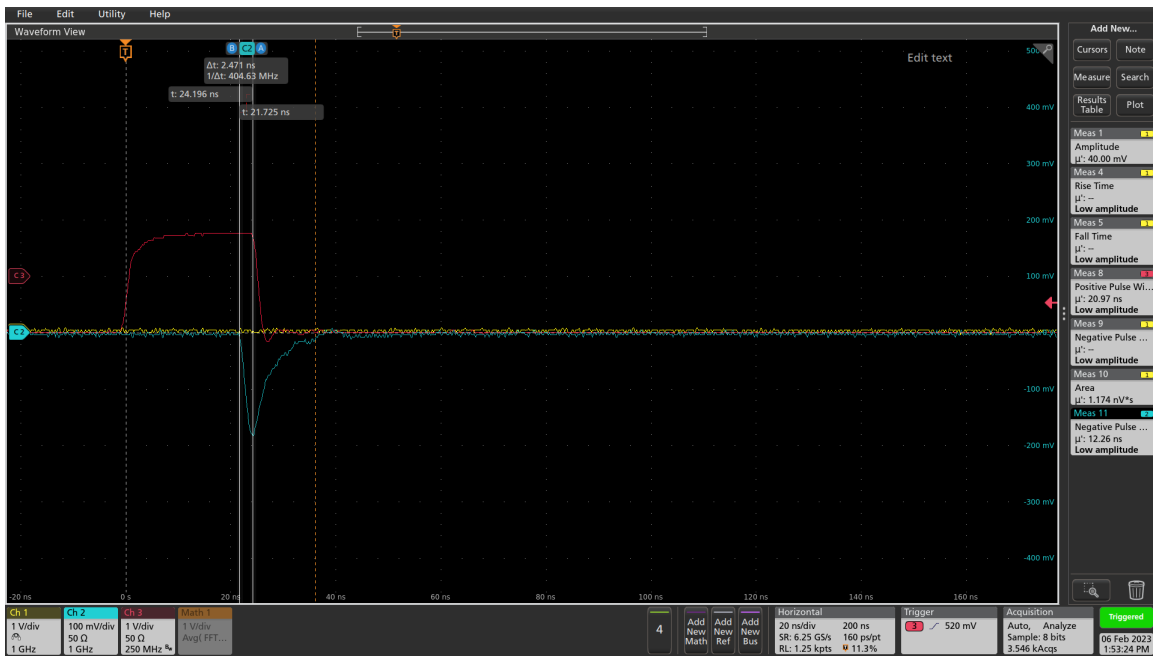


Figure 30: Pulsing Circuit With No Inductor and Resistor

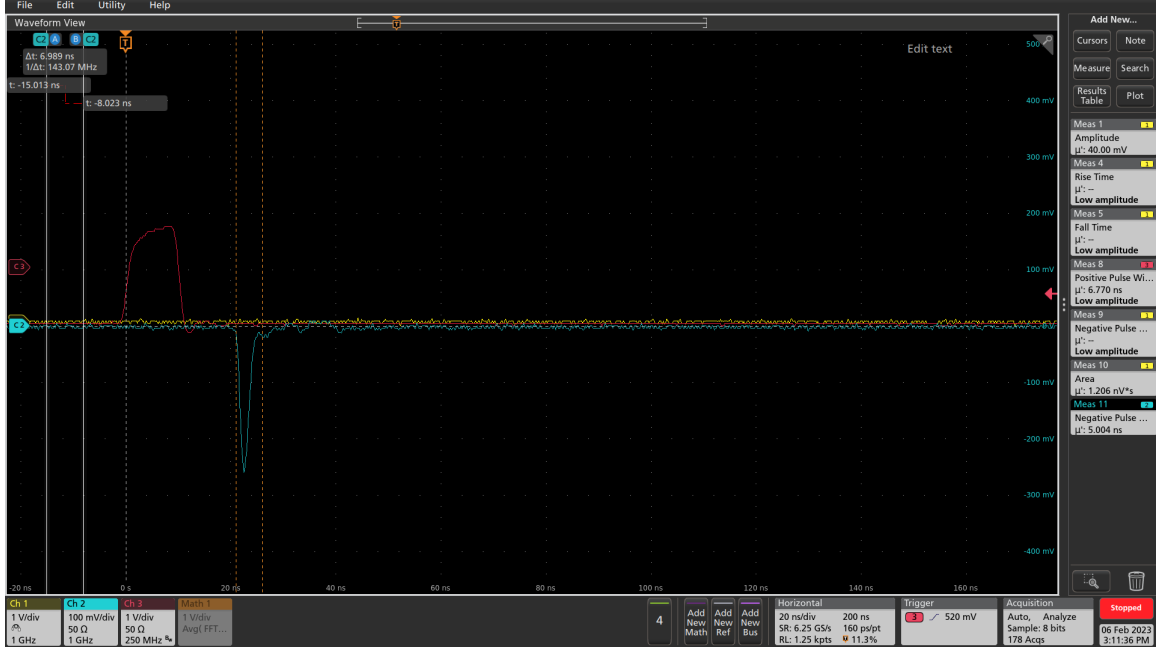


Figure 31: Pulsing Circuit With Inductor and Resistor

522 employing the EPC8004 switch, another utilising the EPC2012 switch, a third using the
 523 same high-speed transistor (BFR92) as implemented in the legacy system, and a fourth vari-
 524 ant incorporating an EPC2012 gate in a through-hole package instead of the standard 0805
 525 surface-mount footprint. Further evaluation was also performed using the latest pulser board
 526 prototype once they had arrived.

527 Following comparative performance evaluations, the configuration using the EPC8004
 528 switch was selected for continued use. While both the EPC8004 and EPC2012 switches
 529 exhibited similar electrical characteristics, the EPC8004 offered superior performance due to
 530 its lower parasitic capacitance, without any additional cost. The pulser board assembly was
 531 housed within a dark box during testing, and a 3D-printed fibre coupler was employed to
 532 facilitate light delivery. The initial focus of the evaluation was on the shape of the generated
 533 optical pulse. During component selection, it was observed that the LED previously sourced
 534 from Mouser (ATS2012UV385 by Kingbright) provided acceptable performance in terms of
 535 electrical characteristics, but the optical output was suboptimal, as it was showing a strange
 536 “double pulsing”, which can be seen in Figure 32. Additionally, this LED was found to be
 537 out of stock and obsolete at the time after testing, precluding further procurement.

538 Subsequently, four ultraviolet LEDs from LC LED were assessed—two emitting at 365 nm
 539 and two at 395 nm—each in both 0805 and 0603 surface-mount packages. Results demon-
 540 strated that the 0805 package LEDs provided significantly better optical coupling efficiency
 541 with the FP400URT optical fibre. Furthermore, the 365 nm variant exhibited superior opti-
 542 cal power output relative to the 395 nm counterparts. Based on these findings, the LC LED
 543 UT-67UV365P [15] 365 nm LED was selected as the most suitable LED for this application.
 544 Tests showed the LED was behaved well, providing an optical pulse of 2.8 ns width, with
 545 3.3 ns eletrical signal, as shown as Figure 33. The pulse width deviation is 60.218 ps, or
 546 2.12% , and the histogram shows the pulse distribution.

547 A long-term stress test was also performed for this LED. The pulser system was placed
 548 in a small dark box, and a new 365 nm LED was soldered onto the pulser board. The pulse
 549 frequency was set to 30,000 Hz, and the pulse width was set to 2.8 ns pulse width, which
 550 yielded a 6.8 ns pulse after dispersion through 180 m of fibre. The system was running

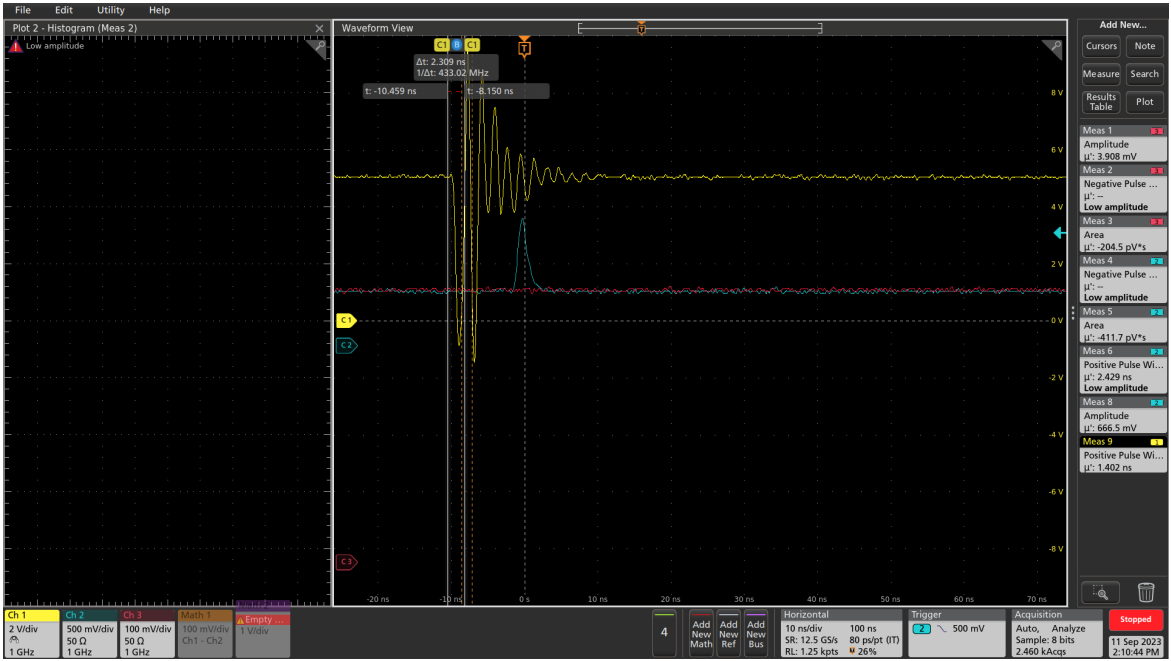


Figure 32: Double pulse observed from the Kingbright ATS2012UV385 LED.

551 continuously for 13 days, during which power and air temperature measurements were made
 552 every 10 seconds. The air temperature was measured at the power meter, using the Thorlabs
 553 PM100USB. Each individual LED is expected to run at around 0.0082 Hz, as the auto-calib
 554 process is expected to pulse any channel at 1 Hz rate and there are 122 active channels. This
 555 means that pulsing the LED at 30 KHz for 13 days is equivalent to 106,849 years of normal
 556 running, not including the short dedicated calibration runs where the system will run at
 557 1 kHz. While we have not calibrated the temperature gain, we are estimating a 1.5% loss if
 558 we compare the same temperature from the beginning of the experiment to the end. **ADD**
 559 **PLOT FOR THIS**

560 7.4 LVDS to TTL Converter

561 The DS90C402 [16] from Texas Instruments was selected as the LVDS-to-TTL conversion
 562 solution. This device is a dual-channel converter, chosen primarily for its fast switching
 563 characteristics—offering both rise and fall times of approximately 500 ps. It operates at
 564 5 V and provides 5 V TTL output levels, which aligns well with the requirements of the
 565 downstream switching circuitry. The inclusion of two channels is particularly advantageous,
 566 as it enables the generation of sub-nanosecond differential pulses by precisely offsetting the
 567 channels, as described in Switch Selection. Among commercially available devices with
 568 these specifications, the DS90C402 is the fastest and is readily available through multiple
 569 distributors.

570 The associated circuit was implemented in accordance with the manufacturer's recom-
 571 mendations provided in the datasheet. A decoupling capacitor was placed in close proximity
 572 to the power supply pin to minimise voltage ripple. Output traces were routed using polygon
 573 fills to reduce impedance and enhance signal integrity, and a continuous ground plane was
 574 placed beneath the signal layers to improve shielding and minimise electromagnetic interfer-
 575 ence. The schematic for this is given in Figure 34.

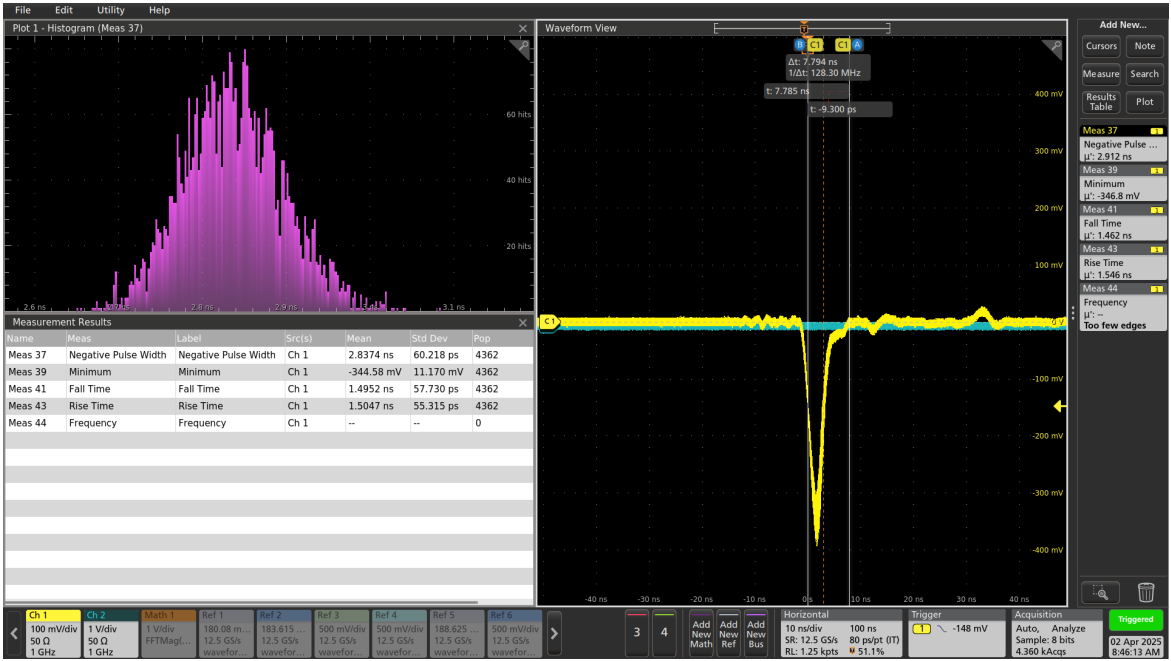


Figure 33: Scope trace and pulse width histogram for a 3.3 ns input signal, through a 1 m FP400URT fibre.

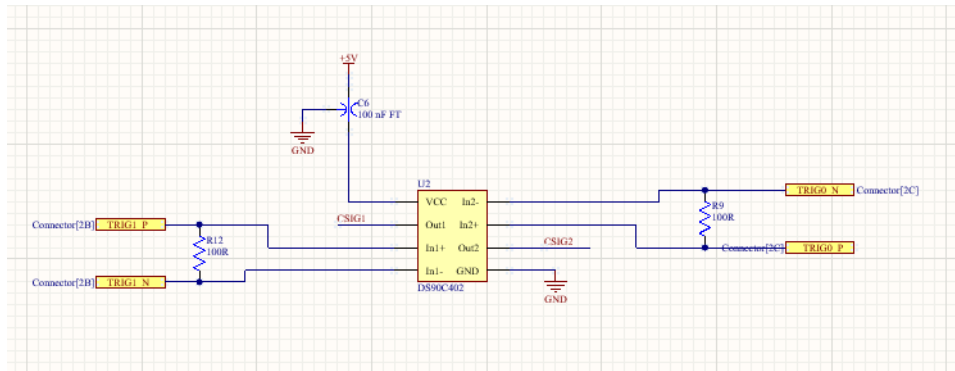


Figure 34: LVDS-TTL Converter Schematic

576 7.5 Power Supplies

577 Each pulser board is required to incorporate a variable voltage power supply dedicated
 578 to driving the LED, with an adjustable output range from 3 V to 12 V. This supply is
 579 used exclusively to modulate the LED’s light output by varying the forward voltage, and
 580 consequently the current. The design specification also necessitates that the power supply
 581 be remotely controllable—i.e., capable of being switched on or off via a simple logic-level
 582 signal.

583 For this purpose, the LT1963A [17] adjustable low-dropout linear regulator was selected.
 584 This regulator has demonstrated reliable performance in previous pulser board iterations
 585 and offers a favourable balance of cost-effectiveness and controllability. The implementation
 586 includes standard filtering and decoupling, with layout details provided in Figure 35. The
 587 schematic provided in Figure 36 is an early version used for prototyping; the adjustable
 588 circuit has been simulated and will be tested shortly, and the enable circuit has been tested,
 589 modified and simplified. Updated schematics will be provided with v1.0 circuit. There will
 590 be overcurrent protection built in to the system as well. A ZXCT1051 (Reference!) is used

591 to monitor the current and if it senses larger than normal current then it send a signal to
 592 the FPGA to turn the damaged board off. A surface mounted fuse will be added in line as
 593 well to make sure there is a second line of defense as well.

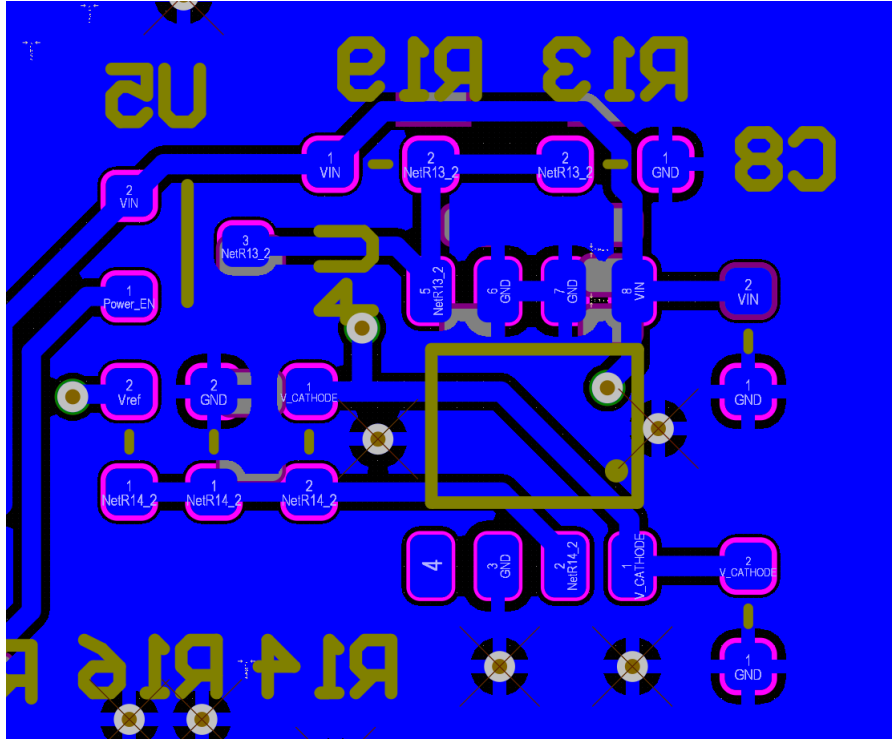


Figure 35: LT1963 Layout

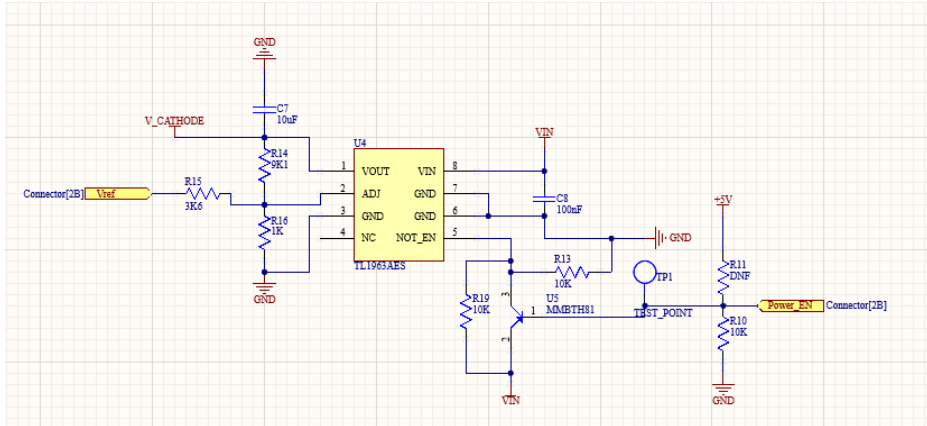


Figure 36: 12V Circuit Schematics

594 In addition to the variable LED supply, each board requires a stable 5 V supply to power
 595 both the DS90C402 LVDS-to-TTL converter and the LMG1020 gate driver. Unlike the LED
 596 supply, this rail remains continuously powered. The 5 V supply is provided by an LM2937-5
 597 [18], a fixed-output linear voltage regulator, which has been successfully employed in various
 598 high-speed and low-noise applications within the laboratory. The associated circuit schematic
 599 and layout and schematic are shown in Figures 37 and 38 respectively.

600 To meet system-level design constraints, each pulser board is equipped with its own
 601 independent 12 V input supply, ensuring that LED output intensity can be individually

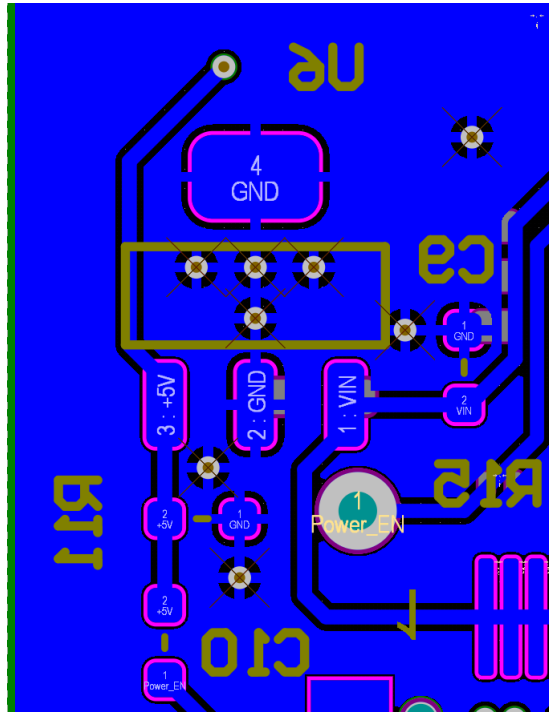


Figure 37: LM2937-5 Layout

controlled on a per-board basis. However, the 5 V supply is common across all boards and derived locally on each pulser module. This approach allows for localised filtering and minimal power distribution path lengths, reducing the risk of noise coupling and voltage drop considerations that are particularly critical in high-speed circuit applications.

Power is supplied to each board via the Eurocard backplane. The 12 V input from the Eurocard simultaneously feeds both the variable (LED) and fixed (logic) power regulators on the pulser board. The LED enable function is controlled via a 5 V logic signal originating from the Eurocard's GPIO interface. Additionally, a DAC output from the Eurocard provides a voltage control signal to the adjustment pin of the LT1963A regulator on each pulser board, thereby allowing precise, programmable control of light intensity.

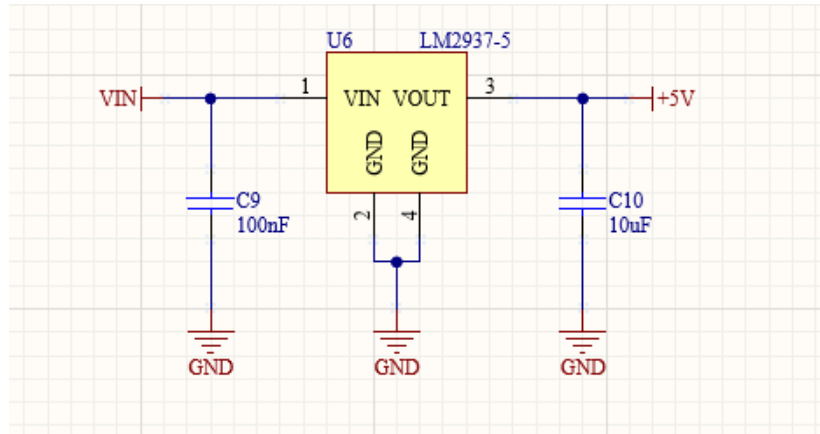


Figure 38: 5V circuit schematics

612 7.6 Connector

613 The previous board connector was deemed too bulky and expensive for the larger number
 614 of channels needed in this system, leading to the process of finding a more suitable alterna-
 615 tive. Following an evaluation of commercially available options, the Phoenix Contact female
 616 connector 1331962 [19] was selected. This connector offers several advantageous specifica-
 617 tions: it is rated for 500 V, features a low contact resistance of $40\text{ m}\Omega$, supports a maximum
 618 current of 0.5 A, and is capable of signal transmission up to 20 Gbit s^{-1} . In addition, it is
 619 cost-effective, priced at approximately £0.50 per unit, with wide availability ensuring ease
 620 of procurement. Multiple height variants are available within the same series, facilitating
 621 flexible mechanical integration within the Eurocard crate system. The compact footprint of
 622 the connector allows for a reduced PCB form factor. Electrically, the high-frequency perfor-
 623 mance supports reliable LVDS signal transmission. Additionally, the compact footprint of
 624 the connector is well-suited to space-constrained PCB layouts.

625 An illustration showing the connector and corresponding circuit layout is provided in
 626 Figure 39.

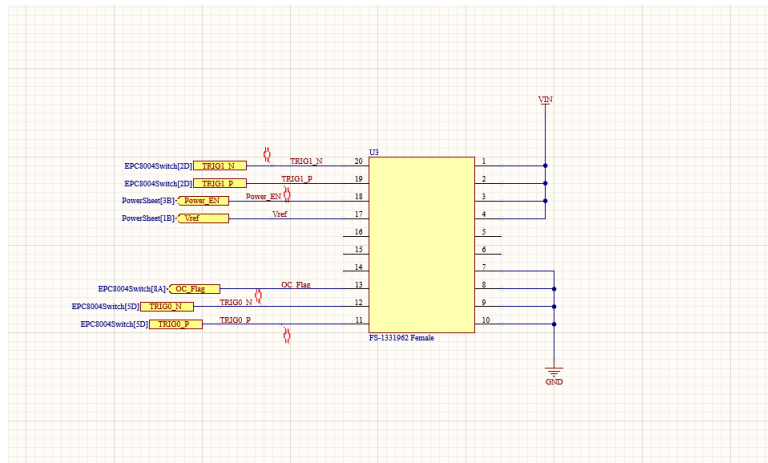


Figure 39: Connector Schematics

627 7.7 Fibre Coupler

628 During the prototyping phase, improvements were made to the PCB layout to better ac-
 629 commodate a fibre coupler. As a result, the current design includes provisions for precise
 630 mechanical mounting and alignment. Specifically, two mounting holes for M2 screws have
 631 been incorporated, enabling the 3D-printed coupler to be firmly secured to the board (see
 632 Figure 40). In addition, two dowel holes have been added to guide the coupler into posi-
 633 tion, ensuring accurate alignment over the LED. Given the tolerances associated with PCB
 634 fabrication and 3D printing, an alignment accuracy of approximately $100\text{ }\mu\text{m}$ is expected.

635 To optimise the electrical path, capacitors have been repositioned as close as possible to
 636 the LEDs. This minimises parasitic inductance and resistance, while enabling a centralised
 637 layout of larger components. The resulting configuration creates a compact chamber housing
 638 both the LEDs and associated capacitors.

639 The design for the fibre coupler is modular, consisting of three components: a base
 640 section mounted to the pulser PCB, a top section into which the fibres will be epoxied, and
 641 an intermediate attenuator element. The latter part will be added to the current design to
 642 space the fibre from the LED and thereby adjust the optical coupling efficiency to achieve
 643 required attenuation, accounting for the different lengths of fibre in the system. This means



Figure 40: Fibre Coupler Design

644 the attenuation will be implemented within the coupler itself, allowing the LED output to
645 remain within the electronically controlled dynamic range.

646 The fibre coupler will be fabricated via stereolithography (SLA) using a black resin to
647 minimise light transmission through the material. Additional light-tight testing will be
648 conducted, and black paint may be applied if further sealing is required. Furthermore, laser-
649 cut rubber gaskets will be introduced at interface points to ensure optimal optical isolation
650 and mechanical sealing.

651 **7.8 Photon Yield Tests**

652 tests on maximising photon yield and available dynamic range should be fully described here

653 **7.9 Production**

654 Production will be carried out using PCB Train as they are local and competitively priced,
655 and known to produce boards of good quality. Estimated cost is £12.27 per board, which
656 equates to £1,496.94 for 122 units or £1,840.5 for 150 units, and production is £4073.48 for
657 122 units for 15 days lead time, or £3985 for 150 units at 25 days lead time. The full cost
658 breakdown is shown in Figure 41

659 **7.10 Changes Expected from v0.9 to v1.0**

660 **7.10.1 LED and Switching Circuit**

661 There will be minimal changes to the LED and switching circuit. Changes will be made to
662 the position of the switching devices, placing them slightly closer to each other to reduce
663 transmission line length. The LED will likely remain as the LC LED UT-67UV365P 365nm
664 0805 LED, but further LED tests will be performed. This takes a short amount of time, and
665 may lead to discovering better LEDs in the future which would be easy to swap in due to
666 standardised footprints.

667 **7.10.2 LVDS-to-TTL Converter**

668 No changes are expected to this circuit.

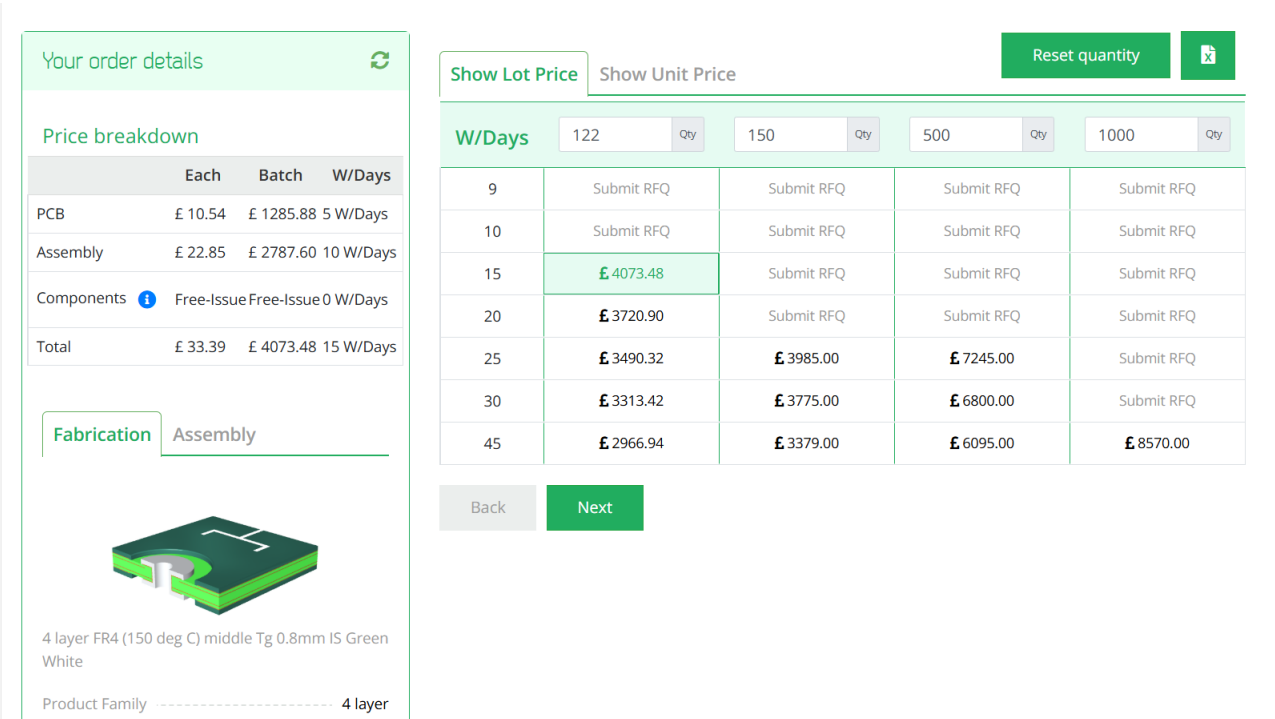


Figure 41: PCBTrain PCB production and assembly costs

669 7.10.3 Power Supplies

670 Reverse voltage bias will be removed as no difference between normal and reverse bias was
671 observed photon output. The overcurrent protection and power enable circuit will be re-
672 worked.

673 7.10.4 Connector

674 No changes are expected to this.

675 7.10.5 Fibre Coupler

676 A brand new fibre coupler will be designed due to the recent requirement changes regarding
677 the different fibre lengths.

678 8 Server Rack and Cooling

679 To house the electronics for the LI systems, two 42U server racks with 800 mm depth will
680 be used. The front of the server rack will be used for electrical connections and displays,
681 and the reverse/internal will be used only for fibre routing. The server racks will include
682 Uninterruptible Power Supplies (UPS) for safe power delivery and for power processing, to
683 avoid issues with potential instabilities in the main power supply. Each rack will include an
684 air conditioning unit to have a controlled temperature and remove humidity from the air,
685 as the relative humidity in the air is expected to be above 70%. Although specific tests on
686 running the LED electronics in humid conditions have not been carried out, it is known that
687 the optical switches for the laser calibration system requires lower humidity levels. In order
688 to simplify things and remove the potential of humidity issues with the LED electronics,

689 both server racks will be air conditioned. These systems are widely available and will be
690 chosen closer to installation.

691 9 LED Monitoring

692 To monitor the light output from the LEDs before attenuation by fibres and convolution
693 with water parameters, PMTs will be placed near to the LED sources. This is a similar
694 design to what is currently used in the Super-K UKLI system. Each LED connector will
695 feature a second fibre to take light to a series of PMTs, which are expected to be Hamamatsu
696 H10721-210. Due to the 8 mm diameter of the PMT window, up to 16 fibres can be attached,
697 meaning one PMT can monitor up to 16 LED boards at once. Each PMT will be powered
698 by a unique low cost power supply developed for the SK UKLI system. These will be housed
699 in a small 2–3 U server rack. The signals from the PMTs will then go to the dedicated HK
700 electronics channels that are set up for monitoring.

701 10 Control System for LEDs

702 The LEDs are driven by a differential LVDS signal originating from the FPGA. The FPGA
703 in use is the Genesys 2 [20] development board, which operates a pulsing VHDL module
704 clocked at 300 MHz. Pulses are generated on the rising edge of this clock, and toggling the
705 output (i.e., asserting and then deasserting the trigger) requires a minimum of two clock
706 cycles. Consequently, the shortest achievable pulse duration in this configuration is 3.3 ns.

707 One of the main limitations of this setup is the coarse time resolution: pulse durations
708 are effectively constrained to integer multiples of 3.3 ns. To achieve a broader and more
709 finely resolved spectrum of optical injection into the detector, improved temporal precision
710 is necessary. This is accomplished using the Xilinx `IODELAY` primitive, originally designed for
711 high-speed interface timing alignment. The `IODELAY` module permits fine-tuning of signal
712 timing to account for PCB trace mismatches, and in this application, it is repurposed to
713 introduce controlled delays between pulses.

714 To generate shorter pulses, two identical signals are created, one of which is delayed
715 using `IODELAY`. These signals are then combined using a logical `AND` operation, producing
716 a narrower pulse. Since the `IODELAY` module requires one clock cycle to process the input,
717 both signals—regardless of whether they are delayed—must pass through an `IODELAY` stage
718 to ensure temporal synchronisation.

719 Conversely, to produce longer pulses, the same methodology is applied, but the signals are
720 combined using a logical `OR` gate instead. This approach extends the pulse width beyond the
721 base clock resolution, enabling pulse durations ranging from approximately 1.5 ns to 4.5 ns
722 in 49 discrete steps. The lower bound is determined by the threshold of the LVDS-to-TTL
723 converter, which does not respond to pulses shorter than approximately 1.5 ns .

724 For channels using the longest optical fibres, this extended range is sufficient, given
725 the intrinsic dispersion in the fibre optics of around 5 ns. However, shorter fibres require
726 additional pulse shaping. To this end, an additional mechanism is implemented using a `for`
727 loop structure within the FPGA logic. This allows the pulse to persist for multiple clock
728 cycles, effectively producing longer pulses by repetition. However, due to FPGA architecture
729 constraints, each iteration of the loop consumes a clock cycle, necessitating careful timing
730 control. For instance, to produce a 6.6 ns pulse, the loop must be configured for two cycles,
731 accounting for the loop overhead.

732 Further refinement is under investigation through the daisy-chaining of multiple `IODELAY`
733 modules. This would enable sub-nanosecond granularity by introducing additional interme-
734 diate delay steps. While promising, this technique requires further validation and testing.

735 The pulse control data structure is currently under development. There are two types
736 of pulse description considered. In the first option, the software interface would require two
737 parameters per channel: a *coarse* step and a *fine* step, reflecting the approach used in the SK
738 system. The other option would be just a single variable and then simple logic turning that
739 variable into the *coarse* and *fine* step that the internal logic requires. Two hardware modules
740 are planned: one for generating the single shortest possible pulse (to minimise latency), and
741 another for multi-cycle pulses using programmable duration. A selection logic will assess the
742 input and route it to the appropriate module based on the desired pulse characteristics.

743 Each LED channel will be controlled independently, allowing for unique pulse configura-
744 tions across channels. The global trigger will be derived from the system clock, and each
745 channel will pulse in a predefined sequence while triggered from the global trigger. This
746 architecture also supports simultaneous pulsing of multiple channels. Should asynchronous
747 behaviour be required, additional per-channel delay logic can be implemented. Given the
748 five distinct fibre lengths used in the system, each channel group will also include a config-
749 urable delay offset to compensate for propagation time differences. These group delays will
750 be calibrated and fixed, with the option of fine-tuning individual channels post-deployment
751 if necessary.

752 The repetition rate can be adjusted as well, including a single pulse, using external
753 trigger, from 0.001Hz through 1 KHz to multiple megahertz if needed, but the system was
754 only tested up to 30 KHz, as that was a high enough rate to illuminate the power monitor's
755 sensor.

756 The FPGA programming remains in active development. Inter-crate communication
757 protocols and synchronisation are currently under integration and testing.

758 11 Crate Electronics

759 11.1 Overview

760 The system specification calls for control of up to 122 LED channels, significantly exceeding
761 the channel counts used in current systems such as Super-Kamiokande or LUX-ZEPLIN,
762 which the previous generation of pulser boards are used for. To manage this complexity, the
763 design prioritises ease of use, maintainability, and straightforward deployment, particularly
764 given that the server racks will accommodate hundreds of optical fibres.

765 To achieve this, a system concept originally developed by ATLAS collaborators (specifi-
766 cally by Ashley Greenal) has been adapted. The original design utilises a Genesys 2 FPGA
767 integrated into a half-width Verotec KM6-2 [21] Eurocard-compatible crate for testing pur-
768 poses. This concept has been extended to a full 19-inch rack width, enabling the integration
769 of up to 36 pulser boards within a single crate.

770 Each FPGA is capable of interfacing with up to 38 pulser boards, thereby maximising
771 the utilisation of available LVDS differential pairs, with an additional pair reserved for the
772 laser trigger signal. This configuration ensures full use of the Genesys 2's I/O capacity while
773 maintaining flexibility for future expansion.

774 The system architecture consists of three primary components: the Blade (Section 11.2),
775 Backplane (Section 11.3) and Eurocard (Section 11.4). This modular approach ensures
776 scalability and facilitates debugging, replacement, and upgrades. It also provides a robust
777 foundation for managing high channel counts while maintaining signal integrity and synchro-
778 nisation across the system.

779 The system will consist of four crates, which allows for up to 144 pulser boards. The
780 OD diffuser system required 122 boards to run, and the auto-Xenon calibration system is
781 expected to use one or two of the additional boards. This means there will be 20 spare boards

782 available for hot-swapping. These can be further grouped into five sets of four, to have four
783 spare boards for each of the five different fibre lengths. Should issues arise, a local technician
784 can remove the signal and monitor fibres from the broken pulser board, attach them to a
785 spare board, and reconfigure the software to use the spare board for running, all with remote
786 expert guidance. Next time an expert is on site they can do further maintenance or repair
787 if needed.

788 11.2 Blade

789 The Blade is a simple, eight layer board, that has a SEAM-40-06.5-L-10-2-A-K-TR [22]
790 connector which is a direct fit for the Genesys 2's FMC connector. It features a PCIE 16X
791 connector at the edge for connectivity to the Backplane. The PCIE was selected by Ashley
792 Greenal as it is a well documented standard connector and there are a large amount of
793 connectors available that can be bought easily. While PCIE connectors are being used, the
794 PCIE standards for communication are not. This is a very dense PCB with all the differential
795 tracks on it, so buried vias and multiple layers will be used. See Figure 42 for a work in
796 progress version.

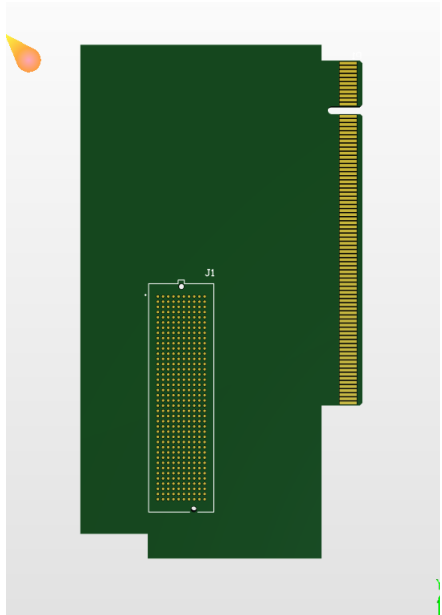


Figure 42: Blade Work in Progress

797 11.3 Backplane

798 The Backplane serves two primary functions: the distribution of differential signals from the
799 Blade to the Eurocards, and the reception and distribution of power throughout the crate
800 system. It accepts external power inputs of 12 V and ± 5 V, and includes a basic regulation
801 circuit to stabilise these supply voltages for downstream use.

802 Given the mechanical constraints and routing complexity, the Backplane is implemented
803 as a four-layer PCB with impedance-controlled traces to ensure signal integrity across all
804 differential pairs. It features a single PCIe x16 connector to interface with the Blade, and
805 three PCIe x8 connectors to interface with the Eurocards.

806 The Eurocards are positioned at slots 2, 8, and 64 within the crate. This arrangement
807 creates two symmetrical chambers with 48 units spacing between cards, ensuring adequate

808 space to accommodate the minimum long-term bend radius of the FP400URT optical fibres.
809 This layout balances mechanical reliability with signal routing efficiency and supports long-
810 term maintainability of the system. See Figure 43 for a work in progress version.

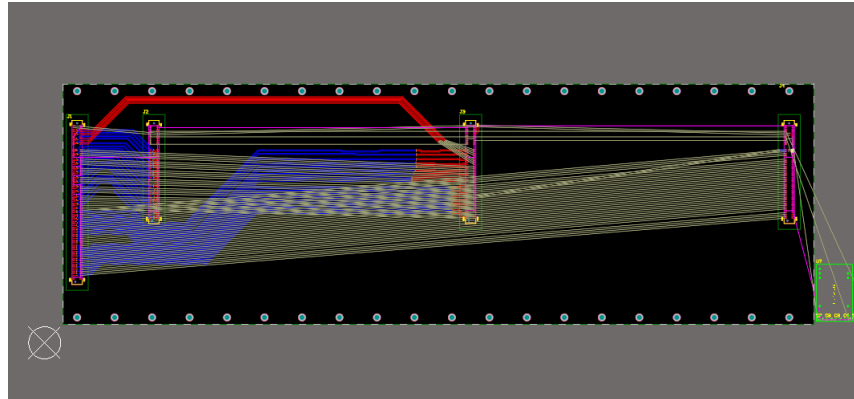


Figure 43: Backplane Work in Progress

811 11.4 Eurocard

812 The Eurocard format defines the physical and electrical standard for the crate system, hence
813 the naming convention. Each Eurocard is equipped with a PCIe x8 connector for interfacing
814 with the Backplane, and is designed to host up to 18 pulser boards—nine mounted on each
815 face. Pulser boards connect via FS-1332120 Male[23] connectors, and each socket includes
816 two mounting holes for mechanical standoffs.

817 The board layout on each side consists of two staggered rows: five sockets in the back
818 row and four in the front. The two faces are laterally offset by approximately 10 mm to
819 prevent interference or fibre clashes when the system is fully populated and enclosed within
820 the crate chamber. This offset ensures smooth fibre routing and accommodates the bend
821 radius requirements of FP400URT fibres.

822 Power distribution within each Eurocard is handled by a THD 12-1212 [24]12 V DC-DC
823 regulator. This regulator provides local power isolation for the pulser boards and includes
824 a control pin connected to a PCA9698 [25] 40-pin GPIO expander. This allows for system-
825 level control, enabling or disabling all pulser boards on a card—an essential feature during
826 power-up, especially when the FPGA may inadvertently drive all differential outputs high
827 during reprogramming.

828 The GPIO expander is responsible for enabling the local 12 V regulator and for selectively
829 powering individual pulser boards. This facilitates fault isolation and power savings in
830 channels that are inactive or disconnected. Additional GPIO pins are assigned to monitor
831 output voltage levels via the overcurrent sensing circuitry.

832 To provide per-channel LED power control, an AD5673 [26] DAC is included. It out-
833 puts analogue control voltages to the onboard adjustable regulators on each pulser board,
834 allowing for independent LED drive voltage per channel. Both the GPIO and DAC devices
835 communicate with the system over the I²C protocol.

836 For laser synchronisation, the Eurocard includes a differential-to-NIM conversion stage.
837 This consists of an LVDS-to-TTL converter identical to that used on the pulser boards,
838 followed by a TTL-to-NIM converter. This ensures compatibility with legacy NIM-based
839 timing systems used in external laser triggering. See Figure 44 for a work in progress version.

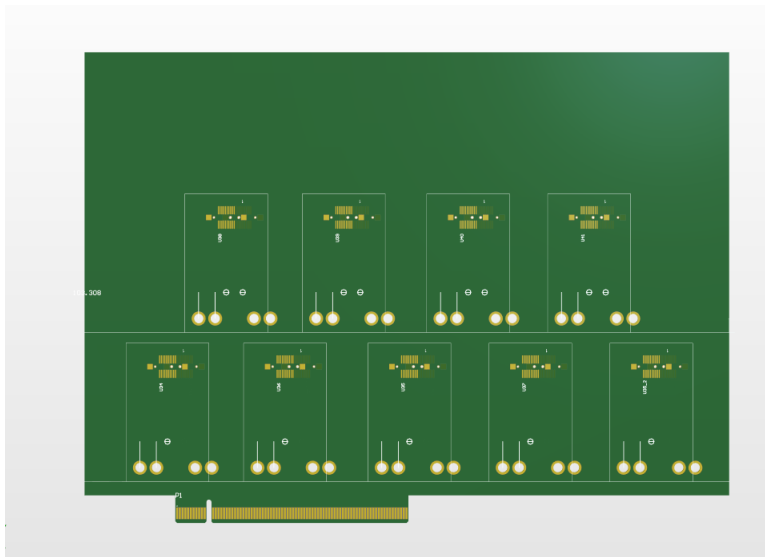


Figure 44: Eurocard Work in Progress

840 12 Conclusions

841 Write this

842 References

- 843 [1] S. Jenkins *et al.*, “HK LI Fibre Specifications,” HK-TN-0091, Aug. 2025.
- 844 [2] Thorlabs. “FP400URT Datasheet.” (2022), [Online]. Available: <https://www.thorlabs.com/drawings/7ade35b092fac3f3-EB2F350-971A-B4B4-29D36C92039FB538/FP400URT-SpecSheet.pdf> (visited on 07/17/2025).
- 845 [3] Hyper-Kamiokande Outer Detector Group: D. Lodovico, E. Drakopoulou, G. Erofeev,
846 *et al.*, “Outer detector technical report,” HK-TN-0064, 2022.
- 847 [4] H.-K. Collaboration. “WCSim Version 1.12.26.” (2018), [Online]. Available: <https://github.com/WCSim/WCSim/releases/tag/v1.12.26> (visited on 09/16/2025).
- 848 [5] S. Boyd *et al.*, “Hyper-Kamiokande light injector diffuser technical note,” HK-TN-0042,
849 May 2023.
- 850 [6] N. E. M. Association. “NEMA STANDARDS PUBLICATION NO. LI 1-1998.” (1998),
851 [Online]. Available: <https://www.nema.org/docs/default-source/standards-document-library/li1.pdf> (visited on 08/19/2025).
- 852 [7] I. T. AG. “BFR 92P E6327 Datasheet.” (2009), [Online]. Available: https://www.mouser.co.uk/datasheet/2/196/Infineon_LNA_BFR92P_14-73949.pdf (visited on 07/17/2025).
- 853 [8] T. I. Incorporated. “LMG1020 Datasheet.” (2018), [Online]. Available: https://www.ti.com/lit/ds/symlink/lmg1020.pdf?ts=1752716909774&ref_url=https%253A%252F%252Fwww.mouser.cn%252F (visited on 07/17/2025).
- 854 [9] N. Braam *et al.*, “LED-mPMTs for hyperK,” HK-TN-0052, Oct. 2023.
- 855 [10] E. P. C. Corporation. “EPC2012 Datasheet.” (2012), [Online]. Available: https://epc-co.com/epc/Portals/0/epc/documents/datasheets/EPC2012_datasheet.pdf (visited on 07/17/2025).

- 866 [11] E. P. C. Corporation. “EPC8004 Datasheet.” (2023), [Online]. Available: https://epc-co.com/epc/Portals/0/epc/documents/datasheets/EPC8004_datasheet.pdf (visited on 07/17/2025).
- 867 [12] Kingbright. “ATS2012UV385 Datasheet.” (2021), [Online]. Available: <https://www.mouser.co.uk/datasheet/2/216/ATS2012UV385-1374632.pdf> (visited on 07/17/2025).
- 868 [13] H. P. K.K. “H10721-210 Datasheet.” (2024), [Online]. Available: https://www.hamamatsu.com/content/dam/hamamatsu-photonics/sites/documents/99_SALES_LIBRARY/etd/H10720_H10721 TPM01062E.pdf (visited on 07/17/2025).
- 869 [14] E. P. C. Corporation. “Design of High Current Nanosecond Resonant Pulse Drivers for Laser Diodes, Lidar, and other Applications.” (2025), [Online]. Available: <https://epc-co.com/epc/Portals/0/epc/documents/application-notes/AN032%20Design%20of%20High%20Current%20Nanosecond%20Resonant%20Pulse%20Drivers.pdf> (visited on 07/17/2025).
- 870 [15] L. LED. “ut-67uv365p Datasheet.” (2018), [Online]. Available: <https://www.lc-led.com/products/ut-67uv365p.html> (visited on 08/21/2025).
- 871 [16] T. I. Incorporated. “DS90C402 Datasheet.” (2013), [Online]. Available: <https://www.ti.com/lit/ds/symlink/ds90c402.pdf> (visited on 07/17/2025).
- 872 [17] A. Devices. “LT1963 Datasheet.” (2021), [Online]. Available: <https://www.mouser.co.uk/datasheet/2/609/lt1963a-2256452.pdf> (visited on 07/17/2025).
- 873 [18] T. I. Incorporated. “LM2347-5 Datasheet.” (2014), [Online]. Available: <https://www.ti.com/lit/ds/symlink/lm2937.pdf> (visited on 07/17/2025).
- 874 [19] P. Contact. “1331962 Datasheet.” (2025), [Online]. Available: <https://www.phoenixcontact.com/en-us/products/smd-female-connectors-fs-0635-20-fv-r-40-1331962?type=pdf> (visited on 07/17/2025).
- 875 [20] Digilent. “Genesys 2 Datasheet.” (2017), [Online]. Available: https://digilent.com/reference/_media/reference/programmable-logic/genesys-2/genesys_2_rm.pdf?srsltid=AfmB0orhD9699F1FTC059o719HmCW-0XnE0RnRJf6Thzcvu0vMs-pbAf (visited on 07/17/2025).
- 876 [21] Verotec. “Verotec KM6-2 Datasheet.” (2017), [Online]. Available: <https://www.verotec.co.uk/tech-downloads/Section%201%20-%20KM6-II%20Subracks.pdf> (visited on 07/17/2025).
- 877 [22] Samtec. “SEAM-40-06.5-L-10-2-A-K-TR Datasheet.” (2025), [Online]. Available: https://suddendocs.samtec.com/catalog_english/seam.pdf?_gl=1*1soskal*_gcl_au*0DQwODM2MjE4LjE3NTI3NDg2NTY.*_ga*MTAxNjAxOTQwNS4xNzUyNzQ4NjU2*_ga_3KFNZC07WW*cxE3NTI3NDg2NTUkbzEkZzAkddE3NTI3NDg2NTUkajYwJGwwJGgw (visited on 07/17/2025).
- 878 [23] P. Contact. “1332120 Datasheet.” (2025), [Online]. Available: <https://www.phoenixcontact.com/en-us/products/smd-male-connectors-fs-0635-20-mv-r-50-1332120?type=pdf> (visited on 08/21/2025).
- 879 [24] T. E. AG. “THD 12-1212 Datasheet.” (2025), [Online]. Available: https://www.tracopower.com/sites/default/files/products/datasheets/thd12_datasheet.pdf?t=1752706801 (visited on 07/17/2025).
- 880 [25] N. B.V. “PCA9698 Datasheet.” (2010), [Online]. Available: <https://www.nxp.com/docs/en/data-sheet/PCA9698.pdf> (visited on 07/17/2025).

- 910 [26] A. Devices. “AD5673 Datasheet.” (2020), [Online]. Available: <https://www.analog.com/media/en/technical-documentation/data-sheets/ad5673r-5677r.pdf>
911 (visited on 07/17/2025).
912